

Technical University of Munich
Physics department



Master thesis
in Nuclear, Particle and Astrophysics

TRISTAN Fly High - Design Studies for a CubeSat Compton Telescope

Matthias Meier

December 2nd, 2019



Max Planck Institute
for Physics

Supervisor:
Prof. Dr. Susanne Mertens

Primary reviewer: Prof. Dr. Susanne Mertens
Secondary reviewer: Prof. Dr. Stephan Paul

Abstract

Astrophysical objects with a large mass-to-size ratio are referred to as compact objects, e.g. black holes, white dwarfs, neutron stars. Many questions concerning these astrophysical objects are still not answered yet. The possibilities to investigate the structure of compact objects are strongly limited. With optical methods, it is hardly possible to resolve the geometry of these object because of their small size to distance ratio. Therefore, other methods have to be developed to compensate for the missing results of classical imaging. The objective of the CubeSat mission ComPol is to investigate the black hole binary Cygnus X-1 for one year. The goal is to improve its physical model by measuring spectrum and polarization in the hard X-ray range. The information about the polarization can be extracted from the kinematics of Compton scattering.

The destined detector system is a Compton telescope made up of two detector layers. The first detector layer, a **Silicon Drift Detector (SDD)**, acts as a scatterer for the incoming photons which are subsequently absorbed in the second layer, a crystalline CeBr_3 calorimeter. The SDD has been primarily developed for the TRISTAN project, a planned detector upgrade of the KATRIN experiment, to search for sterile neutrinos.

The focus of this thesis is a detailed sensitivity study based on Geant4 simulations. It provides a basis for the detector design of ComPol with respect to its polarimetric performance. Possible interaction types and their rates are discussed for the signal events. The event selection is performed and compared for the situation with and without background. Furthermore, the impact of the detector response on the polarization signal is discussed. With the assumed set-up, it turns out that the impact of the position resolution is approximately 6 times larger than the one from the energy resolution. The final sensitivity is determined with the **Minimum Detectable Polarization (MDP)** parameter and verified with a χ^2 -test. Both methods yield a polarization sensitivity of 13% for a one year observation. The analysis is done with regard to the detector response, the considered energy range, and the background radiation. The background turns out to be crucial for the final sensitivity. A **Signal to Noise Ratio (SNR)** of 0.34 is determined from the simulations. This already reduces the sensitivity after one year by 7% degree of polarization. The importance of a large SNR, demonstrated in this work, will guide the design of the shielding concept for the final CubeSat mission. Preliminary studies show that an improvement by a factor of 2 seems feasible.

Contents

1 Compton telescopes	1
1.1 Photon interactions with matter	1
1.1.1 Photoelectric effect	1
1.1.2 Compton scattering	2
1.1.3 Pair production	5
1.2 Working principle of a Compton telescope	5
1.2.1 Event reconstruction	5
1.2.2 Polarimetry	7
1.3 History of Compton telescopes	10
1.4 Conclusions	10
2 ComPol (Compton Polarimeter)	11
2.1 Scientific motivation	11
2.2 CubeSats	17
2.3 Set-up	18
2.3.1 TRISTAN detector	20
2.3.2 CeBr ₃ calorimeter	24
2.3.3 Detector resolutions and energy limits	25
2.4 Conclusion	27
3 Sensitivity study	29
3.1 Introduction to Geant4	29
3.2 Simulation settings	30
3.3 Detector response	32
3.4 Signal simulation	35
3.4.1 Interaction types in the SDD	35
3.4.2 Interaction types in the calorimeter	40
3.4.3 Rate analysis	44
3.4.4 Event selection	46
3.4.5 Polarization analysis	51
3.5 Background simulation	53
3.5.1 Background sources	53
3.5.2 Background exclusion	53

3.5.3 Remaining background events	56
3.5.4 Rate analysis	58
3.6 ComPol's polarization sensitivity	60
3.6.1 Determination of the sensitivity	60
3.6.2 Effects of the detector response on the sensitivity	63
3.6.3 Energy dependence of the sensitivity	63
3.6.4 Impact of the background on the sensitivity	65
3.7 Conclusions	66
4 Summary and outlook	67
A Geometry description for the Geant4 simulation	69
B Normalization of the simulation results	75
C Energy spectra of both detectors	77
C.1 Monoenergetic photon sources	77
C.2 Photon source with spectrum of Cygnus X-1	82
C.3 Background spectra	84
Bibliography	87

"Look up at the stars and not down at your feet. Try to make sense of what you see, and wonder about what makes the universe exist. Be curious." - Stephen Hawking [1]

Chapter 1

Compton telescopes

With Compton telescopes it is possible to measure the energy of incoming X-rays and to reconstruct the position of the source. These telescopes are used for astrophysical purposes as well as nuclear medicine or nuclear radiation detection. By using the well known kinematics of Compton scattering it is even possible to determine the polarization of the radiation.

This chapter introduces the different possible interactions between photons and matter, especially focusing on Compton scattering. Afterwards the working principle of Compton telescopes is explained (section 1.2) and finally section 1.3 gives an overview of the history of Compton telescopes.

1.1 Photon interactions with matter

The interaction of light with matter depends on the energy of the photon and the properties of the matter. The photoelectric effect and Compton scattering are the dominant processes in the X-ray energy range. Pair production becomes dominant for the gamma range (> 1 MeV). The cross sections for photon interactions with silicon are shown in figure 1.2 and described in further detail in the following.

1.1.1 Photoelectric effect

The photoelectric effect describes the absorption of a X-ray by the electron shell of an atom. When the photon is absorbed, an electron gets ejected from the shell. A visualization of the process is shown in figure 1.1. The energy of the incoming X-ray has to be larger than the ionization energy of the atom. The cross section increases stepwise when the photon energy E exceeds the binding energy of an electron shell. This is shown in figure 1.2 for the K shell of silicon at 1.84 keV [3].

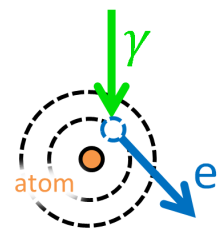


Figure 1.1: Sketch of the photoelectric effect

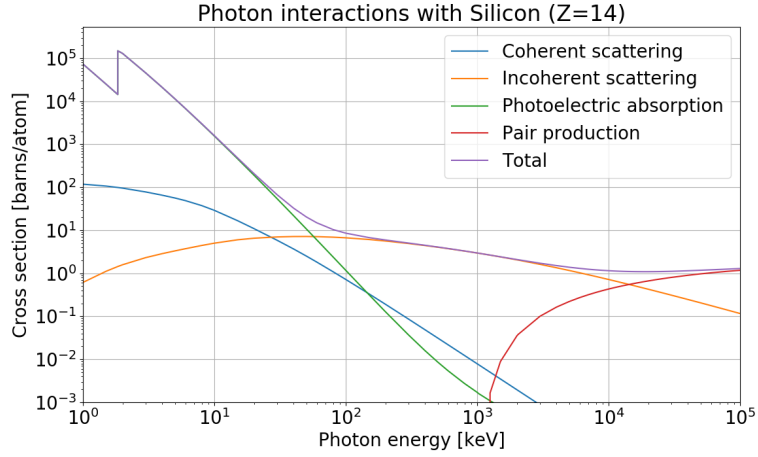


Figure 1.2: Cross sections for photon interactions with silicon. The photoelectric absorption is dominant up to about 100 keV. Compton scattering (Incoherent scattering) is dominant between 100 keV and 10 MeV. Pair production becomes dominant for energies > 10 MeV. Rayleigh scattering (Coherent scattering) contributes only around 10 keV significantly to the total cross section. All data has been taken from the XCOM Photon Cross Sections Database [2].

Photoelectric absorption becomes more dominant for elements with large atomic numbers Z . The cross section scales with Z^5 and $E^{-3.5}$ [4].

1.1.2 Compton scattering

Compton scattering describes the interaction of a photon with a free or nearly free electron ($E_{\text{Ionization}} \ll E_{\text{Photon}}$). The photon transfers some energy to the electron and gets deflected by the angle θ as shown in figure 1.3. The relation between the wavelength shift $\Delta\lambda$ of the photon and the scatter angle θ is given as

$$\Delta\lambda = \lambda_C(1 - \cos\theta) \quad (1.1)$$

with $\lambda_C = h/m_e c$. The minimum energy transfer corresponds to $\theta = 0^\circ$ and the maximum energy transfer to $\theta = 180^\circ$.

The differential cross section for Compton scattering was originally described by Klein and Nishina [5]. Expressed in polar coordinates and averaged over the polarization direction of the outgoing photon, the differential cross section is given by the

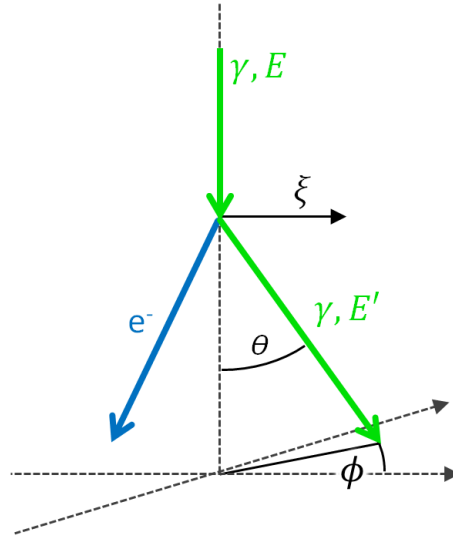


Figure 1.3: Sketch of a Compton scattering process. The incoming photon with energy E and polarization vector ξ transfers energy to an electron. The outgoing photon with energy E' is deflected by θ . The azimuthal angle between the initial polarization vector and the outgoing photon path is called ϕ .

following equation:

$$\frac{d\sigma_{CS}}{d\Omega} = \frac{r_0^2 \epsilon^2}{2} \left(\frac{1}{\epsilon} + \epsilon - 2 \sin^2(\theta) \cos^2(\phi) \right), \quad (1.2)$$

with $\epsilon = \frac{E'}{E}$ denoting the ratio of the energies of the scattered and the initial photon. The classical electron radius is given by r_0 , θ represents the scatter angle, and ϕ the azimuthal scatter angle between the polarization vector ξ of the initial photon and the propagation direction of the scattered photon.

Incoherent scattering

To correctly describe scatter effects in a material, incoherent scattering has to be introduced. That is due to the fact that electrons in a material are bound to atoms and classical Compton scattering applies to free electrons only. When talking about *incoherent scattering* in this work, it is to emphasize the difference to classical Compton scattering. Otherwise, the more common term *Compton scattering* is still used.

The so called incoherent scattering factor S is introduced to correct the differential cross section for the case of bound electrons. The cross section for incoherent

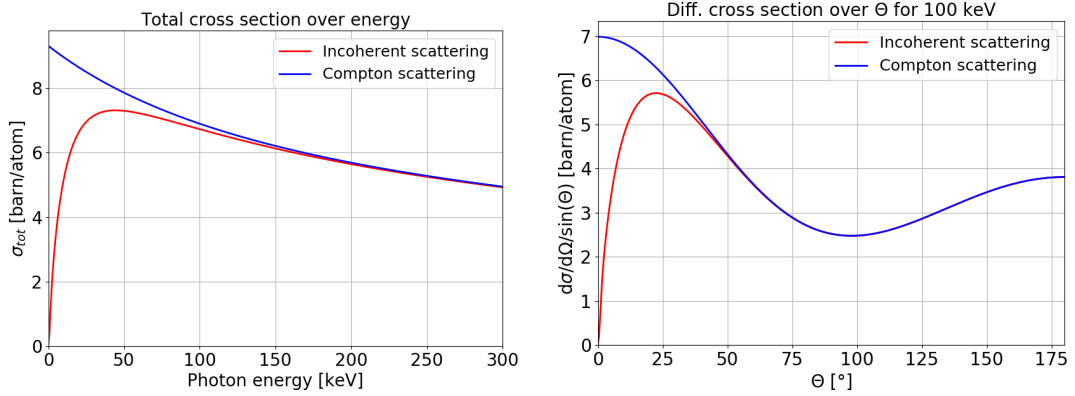


Figure 1.4: Comparison between the cross section for Compton scattering and incoherent scattering (Compton scattering at bound electrons).

Left: Total cross section plotted over the energy of the incident photon.

Right: Differential cross section scaled with $1/\sin(\Theta)$ and plotted over the scattering angle Θ for 100 keV photon energy.

scattering results from the differential cross section for Compton scattering and the correction factor S as follows:

$$\frac{d\sigma_{IS}}{d\Omega} = \frac{d\sigma_{CS}}{d\Omega} \cdot S(E, \theta) \quad (1.3)$$

This correction factor depends on the momentum transfer

$$\Delta p = \sin\left(\frac{\theta}{2}\right) \cdot \frac{E}{hc} \quad (1.4)$$

between photon and electron. Its value corresponds to the number of electrons of an atom that contribute to the scattering cross section. Thus, S is also material dependent. Based on a fit to experimental data, Hubbell et al. [6] determined

$$S_H(E, \theta) = 14 \cdot \frac{1 - \exp(-0.18(E \sin(\theta/2))^{0.87})}{1 + 7.19 \cdot \exp(-3.11E \sin(\theta/2))}. \quad (1.5)$$

The difference between Compton and incoherent scattering mainly appears at small energies and small scattering angles Θ . This behavior is shown in figure 1.4.

1.1.3 Pair production

Pair production plays no significant role in the energy range investigated in this thesis.

It describes the production of an electron and a positron from a high energy photon (see figure 1.5). To conserve momentum, this process only happens in the vicinity of a nucleus or more rarely near an electron. The energy threshold for this process is at 1022 keV, the sum of the rest masses of electron and positron.

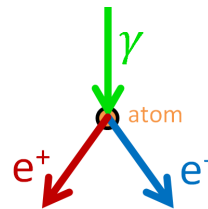


Figure 1.5: Sketch of the pair production process

1.2 Working principle of a Compton telescope

Compton telescopes can be used to measure energy spectrum, position, and polarization of X-ray sources. For imaging it is necessary to reconstruct each event as described in the following section 1.2.1. This reconstruction is needed as a basis for polarization measurements (section 1.2.2). The focus of this thesis is on polarimetry.

1.2.1 Event reconstruction

The simplest set-up of a Compton telescope consists of two parallel detector layers. Both detectors need a spatial and an energy resolution. A simple example of an useful event consists of two interactions. In a first step, the incoming X-ray with energy E interacts via Compton scattering in the first detector layer. The second interaction is the absorption of the X-ray via photo effect in the second layer, the calorimeter. Not all incoming X-rays interact in a way that they can be used for imaging or polarimetry. Only a rather small fraction ($<1\%$) of events is useful for the analysis. A sketch of the detector layers and an exemplary useful event is shown in figure 1.6.

The X-ray deposits the energies E_1 and E_2 at the positions R_1 and R_2 . For Compton scattering, the relation between the wavelength shift of the X-ray and the scatter angle is known (equation 1.1). With the wavelength shift expressed in terms of energy, the following formula results:

$$\frac{1}{E'} - \frac{1}{E} = \frac{1}{m_e c^2} (1 - \cos \theta) \quad (1.6)$$

For our exemplary event we can express the initial energy as $E = E_1 + E_2$ and

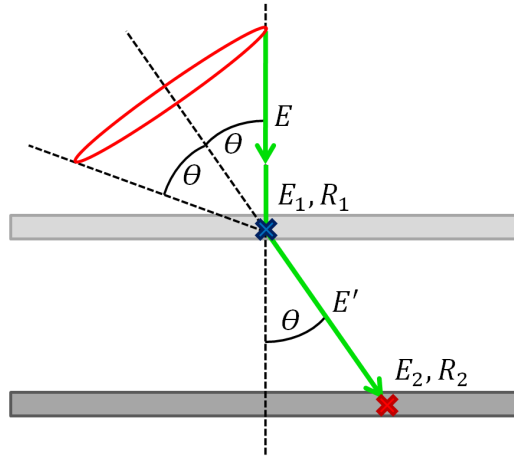


Figure 1.6: Illustration of a Compton telescope with an exemplary two-step interaction of an X-ray (green). The event consists of two interactions, first Compton scattering (blue cross) and subsequent photoelectric absorption (red cross). By analyzing the interaction positions R_i and the corresponding energy deposits E_i with equation 1.7, it is possible to confine the origin of the photon to a cone surface with opening angle 2θ . This cone is indicated by the red circle.

the energy after the Compton scattering as $E' = E_2$, so that the scatter angle is calculated as

$$\cos \theta = 1 - m_e c^2 \left(\frac{1}{E_2} - \frac{1}{E_1 + E_2} \right). \quad (1.7)$$

As we can see, it is possible to confine the X-ray's origin to a cone surface. The tip of the cone is at the position R_1 of the Compton scattering, its symmetry axis is parallel to the path from R_1 to R_2 and its opening angle is 2θ .

The system described so far is a Compton Camera. It is characterized by the fact, that it can observe the entire 4π solid angle. This is possible because the instrument does not necessarily have a front side. As long as the incoming photon scatters in one of the layers and is absorbed in the other one, the origin of a photon can be confined to a cone surface. This is possible for all incoming direction. Yet, for a single event it is not possible to reconstruct the exact origin. To obtain a meaningful direction determination, the possible origins of a statistical significant number of events have to be analyzed. A visualization is shown in figure 1.7.

A Compton telescope cannot observe the whole solid angle. It has an additional optics (e.g. a collimator) in front, to focus on a specific direction. This strongly

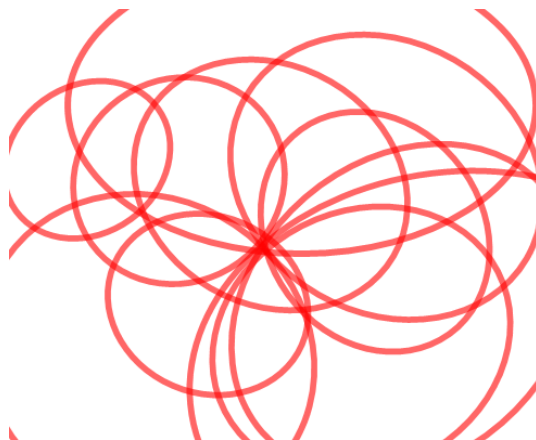


Figure 1.7: Source reconstruction for the operation of a Compton camera. Cuts through the reconstructed cone surfaces for all events get compared in the source plane. X-ray sources are located at the intersections of multiple circles.

improves the background exclusion efficiency. The details on the event selection of ComPol, the Compton telescope studied in this thesis, will be given in section 3.4.4.

The geometry of a Compton telescope can vary a lot from the set-up shown in figure 1.6. It is possible to introduce more layers, to increase the probability of Compton scattering. Another alternative is to arrange the calorimeter around the detector for the Compton scattering. The latter can improve the sensitivity for the polarization. This is based on the dependence of the Compton cross section on the initial polarization and the scatter angle θ (compare section 1.2.2). It would be even possible to use a single block of detector material as long as it is feasible to measure for one event two spatially separated photon interactions and their corresponding energies. The variety of events that can be used for the analysis depends on the detector set-up. For example, in a set-up with more layers, it is more probable to clearly identify an event with multiple Compton scattering before the photon is absorbed.

1.2.2 Polarimetry

With a Compton telescope it is not only possible to do imaging and spectroscopy, the polarization can be determined too. The electric field of electromagnetic radiation is described with a polarization vector for each photon. To obtain the predominant polarization plane and the degree of polarization P of a beam, it is necessary to average over all photons. The polarization plane is parallel to the propagation direction and is specified by the polarization angle Ψ . For astrophysical objects, Ψ is defined as the angle between the North direction and the polarization plane, in-

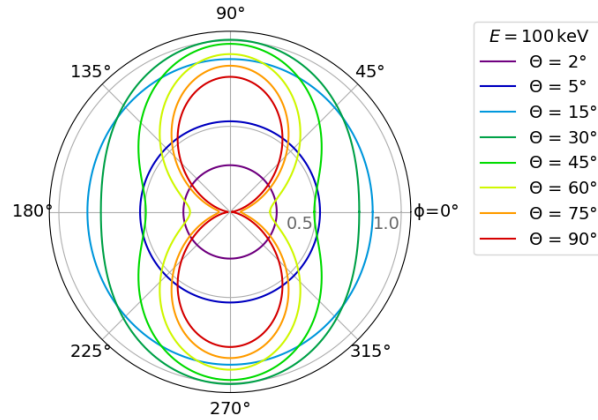


Figure 1.8: Polar plot of the differential cross section for incoherent scattering in silicon according to equation 1.3. Each colored line shows the dependence of the cross section on the azimuthal scatter angle ϕ for a specific scatter angle θ . The azimuthal angle ϕ is with respect to the initial polarization vector. The energy of the incident photons is fixed to 100 keV. The radial distance to the midpoint corresponds to the amplitude in barn/atom.

creasing counter-clockwise when looking in the direction of the source. The degree of polarization describes the relative amount of polarized photons to all detected photons.

To determine the polarization properties of the incoming X-rays, the same events as in section 1.2.1 are analyzed. The X-rays of these events undergo Compton scattering in the first detector plane and photoelectric absorption in the second. The direction of the Compton scattered photon depends on the initial polarization vector. This dependence is described by the $\cos^2(\phi)$ term in the differential cross section for Compton scattering given in equation 1.2. The cross section has its maximum for

$$\phi = 90^\circ \text{ and } \phi = 270^\circ.$$

This means it is more probable for an incident X-ray to be scattered in a direction orthogonal to the initial polarization vector than parallel to it. A precise plot of the differential cross section for incoherent scattering (Compton scattering at bound electrons) and its angle dependence is shown in figure 1.8.

The imprint of the polarization in a measured dataset is visible after the reconstruction of each event as described in section 1.2.1. For every event which is assigned to a source, the azimuthal angle Φ can be calculated. It is chosen relative to an arbitrary reference direction in the instrument. With the knowledge of the orientation of the instrument, it is possible to determine the polarization angle Ψ or translate

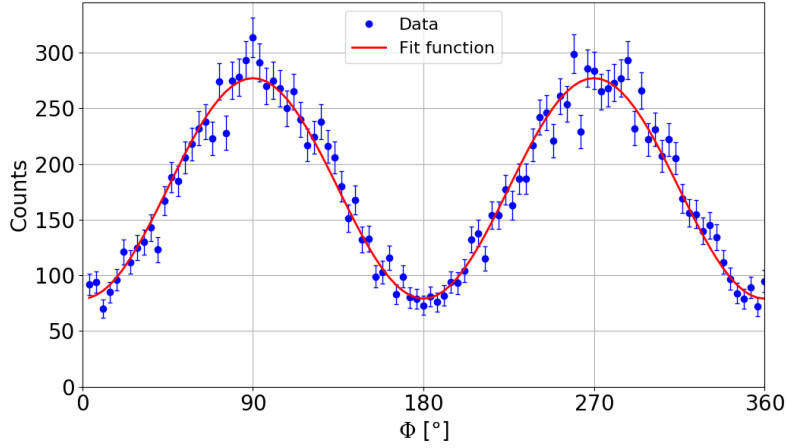


Figure 1.9: Exemplary distribution of the azimuthal scatter angle Φ for polarized photons. The scatter angle Φ is chosen between a reference direction in the instrument and the path of the scattered photon.

the results to any other reference frame. The angle Φ is different to the so far used azimuthal scatter angle ϕ . Both angles describe the polarization dependent direction of the scattered photon. The reference frame for Φ is relative to the instrument whereas the reference frame for ϕ is individually oriented along the path and the polarization vector of each incoming X-ray. An exemplary Φ distribution is shown in figure 1.9. This distribution is described by equation 1.8 [7].

$$f_P(\Phi) = C \cdot [1 + a \cos(2(\Phi - \psi))] \quad (1.8)$$

The parameter C corresponds to the upwards shift of the cosine. It is related to the total number of events. The amplitude of the curve is described by the modulation amplitude a . It corresponds to the absolute amplitude A , divided by C . The sideways shift of the curve is described by ψ and corresponds to the polarization angle in the coordinate system of the instrument. The polarization angle Ψ is obtained by a coordinate transformation from the instrument's coordinate system to the Earth's system.

With equation 1.9 it is possible to determine the degree of polarization P of the incoming radiation. It is equivalent to the ratio of the measured modulation amplitude a to the modulation amplitude μ for 100% polarized light.

$$P = \frac{a}{\mu} \quad (1.9)$$

1.3 History of Compton telescopes

So far, the history of spaceborne Compton telescopes is a rather short story. Two famous telescopes were successfully launched:

- **COMPTEL**

The Compton telescope COMPTEL was launched on board of NASA's **Compton Gamma-Ray Observatory (CGRO)** in April 1991. After 9 successful years of operation and data taking, some technical issues forced NASA to deliberately de-orbit the satellite. It fell into the Pacific ocean in July 2000. COMPTEL was one of four X-ray and gamma ray experiments in the CGRO spacecraft [8]. The telescope covered an energy range from 1 MeV to 30 MeV and had a field of view of about 1 sr. The detector system was made up of two scintillator layers. Their areas were 4300 cm² and 8600 cm². Both layers consisted of several separate modules. The upper layer was made out of liquid scintillator cells and the lower layer out of sodium iodide (NaI) crystals [9].

- **IBIS**

In October 2002, the gamma ray observatory INTEGRAL was launched by the European Space Agency. IBIS (Imager on-Board the INTEGRAL Satellite) and three other instruments are installed in the satellite. IBIS covers an energy range from 15 keV to 10 MeV. The detector system also consists of two layers. The upper detector layer is a semiconductor detector made out of Cadmium telluride (CdTe) with an area of 300 cm². The lower layer is a Cesium Iodide (CsI) scintillation crystal with an area of 2600 cm² [10].

1.4 Conclusions

Compton telescopes can operate simultaneously in different measurement modes: imaging, spectroscopy, and polarimetry. This versatile applicability is advantageous especially for experiments which are interested in more than one of these operating modes. Except for spectroscopy, the respective information is reconstructed from the kinematics of Compton scattering. Therefore, Compton telescopes show the best performance for X-ray energies in the range from $\sim 10^1$ keV to $\sim 10^4$ keV, where Compton scattering is the dominant interaction process of photons with matter. This range depends on the used detector material.

To obtain a good detector performance, it is advisable to carefully choose the detector types. The detectors have to cover the initial photon energies but also the small energies which are deposited during Compton scattering (down to a few percent of the initial energy). A convenient way is a stacked detector system. A low energy detector works as a scatterer for the incoming photons and a high energy detector as an absorber. On this way, it is possible to cover the necessary energy range.

Chapter 2

ComPol (Compton Polarimeter)

ComPol is the abbreviation for **Compton Polarimeter**. It is a CubeSat mission, which aims at measuring the spectrum and the polarization of the black hole binary system Cygnus X-1 in the medium to hard X-ray range (20 keV to 2000 keV) for at least one year. The satellite will fly in a low Earth orbit (~ 500 km). The ComPol collaboration includes a French working group from the CEA (Commissariat à l'énergie atomique) in Paris, a German one from the Max-Planck-Institute for Physics in Munich, with support from the Technical University of Munich, and the Max-Planck-Institute for astrophysics in Garching near Munich.

The physical motivation, the idea of CubeSat missions, and the set-up is described in the following sections 2.1 to 2.3.

2.1 Scientific motivation

The measurement campaign of ComPol is limited due to the small active detector area (see the following sections). The amount of collected data is very small compared to standard satellite missions. To compensate for this fact, ComPol will observe only one source for at least one year. It will simultaneously operate as a polarimeter and spectrometer. The scientific goal behind the ComPol mission is to extend the understanding of the geometry, accretion disk properties, X-ray emission mechanisms, and further characteristics of **Black Hole Binaries (BHBs)**.

A BHB is a **Black Hole (BH)** and a star orbiting each other, while the BH continuously accretes matter from the star. BHs belong to the category of compact objects. These are astrophysical objects with a high mass relative to their size. They often emerge as the final state in the life of a star. Examples for compact objects are BHs, white dwarfs, and neutron stars.

Cygnus X-1 is the astrophysical object, which will be observed by ComPol. It is a BHB in the star constellation of the swan (lat. Cygnus). It is one of the brightest X-ray sources visible from Earth. The distance from Earth is 1.8 kpc [11]. The BH of Cygnus X-1 has a mass of about $16 M_{\odot}$ [12]. The star is a blue supergiant with a mass of about $27 M_{\odot}$ [12]. The orbital period of the system is 5.6 days [13]. BHBs are known for strongly fluctuating spectra. Also Cygnus X-1 can transit through

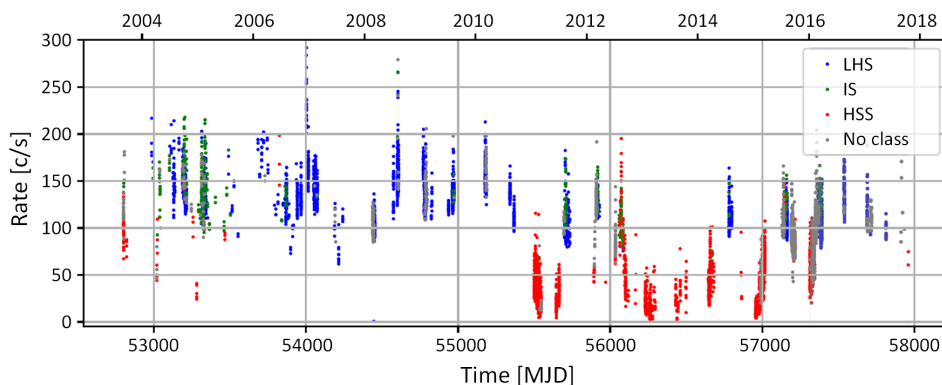


Figure 2.1: Cygnus X-1 transits through several spectral states, Low Hard State (blue), Intermediate State (green), High Soft State (red). Low/High refers to the luminosity of the state and Hard/Soft to the dominant X-ray energy range. The measured overall rate of the LHS is higher than that of the HSS. This is plausible since the nomenclature refers only to the luminosity in the soft X-ray range. Datasets which cannot be classified according to this scheme (precise description by Grinberg et al. [14]) are marked with gray dots. Plot adapted from [15].

several spectral states, the **Low Hard State (LHS)**, the **High Soft State (HSS)**, and an **Intermediate State (IS)** [14]. Sometimes it cannot be clearly assigned to one of these states. During the last 20 years it mainly stayed in the LHS as shown in figure 2.1. Grinberg et al. [14] precisely described this classification. The states are classified by their spectral properties. Low/High refers to the luminosity of the state and Hard/Soft to the dominant X-ray energy range. The energy of maximum emission is at ~ 1 keV for the HSS and at ~ 100 keV for the LHS. The comparison of LHS and HSS spectra is shown in figure 2.2. Both spectra can be interpreted as a combination of spectral components with different weightings, a low energy part (0.5 keV to 10 keV), a high energy part (10 keV to 400 keV), and a hard tail for energies > 400 keV. These emissions can be explained by several effects such as thermal emission, synchrotron radiation, inverse Compton scattering etc. The interplay of these effects is not completely understood. The current LHS models show a better agreement with the data compared to the HSS models. This indicates that not all effects are sufficiently understood.

An illustration of the emission processes for the LHS is shown in figure 2.3. The BH attracts matter from the star, which forms an accretion disk around it. The disk has a thermal emission spectrum with temperatures of a few 100 eV [17]. The production mechanism of the hard X-ray component is more complex. It can be explained

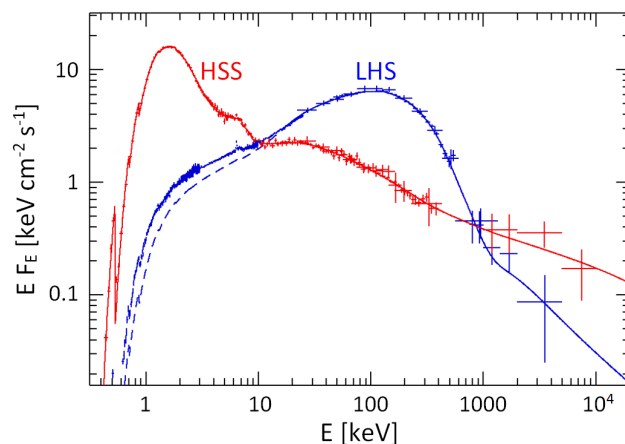


Figure 2.2: Spectra of the two main states of Cygnus X-1, High Soft State (red) and Low Hard State (blue). Low/High refers to the luminosity of the state and Hard/Soft to the dominant X-ray energy range. The maximum emission in the HSS is at ~ 1 keV and for LHS at ~ 100 keV. Plot adapted from [16].

by inverse Compton scattering of soft photons in a hot corona. This hot corona surrounds the BH and the inner parts of the accretion disk. The temperature of the thermal electrons in the corona is approximated to be around 70 keV [15, 17]. Another possible theory for the origin of the hard spectral component is synchrotron emission in jets. Jets form along the rotation axis of such heavy astrophysical objects. A small fraction of the accreted matter does not fall into the BH. It gets accelerated into a spiral jet perpendicular to the accretion disk. The hard photons could originate from synchrotron radiation in the jet formation region. Such jets were already detected in the radio spectrum of Cygnus X-1. Wilms et al. [17] showed a significant correlation between the X-ray and the radio emission of Cygnus X-1. Both explanations predict the origin of the hard spectral component to be in the immediate vicinity of the event horizon of the BH. Additional effects like reflection of coronal photons on the disk and synchrotron radiation in jet regions can produce photons with a large variety of energies.

The physical models for the HSS are less definite than for the LHS. What is certain is that the spectral shape in the HSS does not match with models which imply the presence of a hot corona. Models without a hot corona (see visualization in figure 2.4) show a much better agreement with the data. Until now, it is unclear whether a cold corona is present in the HSS. Without a corona, the disk reaches farther to the BH and a lot more soft photons are directly emitted from the disk. The disk temperature rises for a disk closer to the BH. From experimental data,

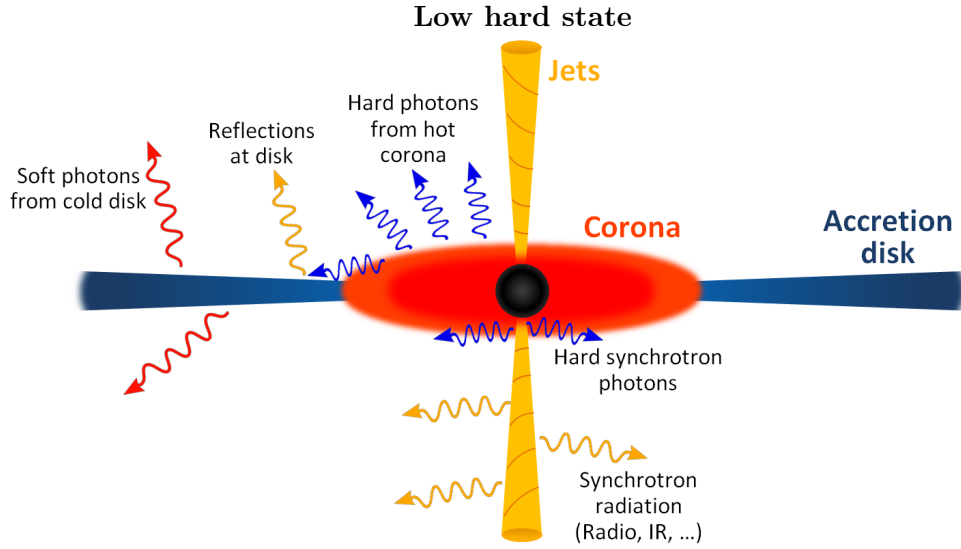


Figure 2.3: Illustration of the geometry and the possible X-ray emission mechanisms of Cygnus X-1 in the LHS. The black hole (BH) is indicated by the black circle in the center. The star of the BHB is not shown. The hard X-ray component of the LHS spectrum can be explained by a hot Corona around the BH. Soft photons from the disk gain energy by inverse Compton scattering at the hot electron plasma inside the corona. Another emission mechanism for hard X-rays is synchrotron radiation in the formation region of jets [15]. The soft component of the LHS spectrum can be explained by thermal emission from the not obscured parts of the rather cold accretion disk.

Wilms et al. [17] determined a temperature value of a few keV for thermal emission from such a disk. Usually, no radio emission is detected during the HSS. Therefore, it can be assumed that there is reduced or even no jet formation. The high energy component of the HSS is still under debate. A possible explanation could be inverse Compton scattering at electrons free-falling into the BH [18].

The hard X-ray tail (> 400 keV) in both states can be explained by synchrotron radiation from jets [19]. These photons are too energetic to be effectively produced by inverse Compton scattering. Another possible explanation would be a hybrid (thermal/non thermal) corona as it is proposed by McConnell et al. [20] or Romero et al. [21]. The data of the INTEGRAL experiment shows a high degree of polarization for the hard tail [19]. Therefore, this tail is most likely generated by synchrotron radiation and not by thermal emission.

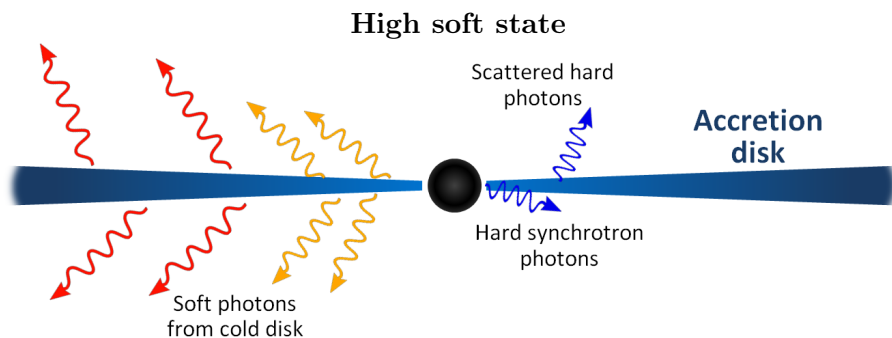


Figure 2.4: Illustration of the geometry and the possible X-ray emission mechanisms of Cygnus X-1 in the HSS. The black hole (BH) is indicated by the black circle in the center. The star of the BHB is not shown. The spectrum in the HSS is dominated by soft photons. This emission can be explained by a reduced or missing corona. The increased area of the uncovered accretion disk enables the emission of low energetic photons directly from the disk. The hard component can be explained by synchrotron radiation in the inner accretion region or by scattering processes in the disk.

A lot of effects have to be considered for a complete model of such a BHB: coronal effects, the geometry of the accretion disk, reflections on the disk, relativistic effects, inclination of the system with respect to the observer, mass and spin of the BH, the accretion rate etc. This large parameter space and the limited observation methods for compact objects make it difficult to determine the correct physical model. There are still many open questions. *What are the actual links between the effects just mentioned and the emitted radiation spectrum? How do transitions between the different states work? What causes these transitions? What is the emission mechanism of the hard power tail?* The key to answering some of these questions are polarization measurements. By measuring the degree and the angle of polarization it is possible to extend the two-dimensional parameter space (spectra and time variability) to a four-dimensional parameter space. As a lot of models predict the measured spectrum but not the same polarization a measurement of the latter allows to exclude certain models.

Polarized radiation can have several origins in a BHB. The main production mechanisms are synchrotron radiation and scattering. For synchrotron radiation, most of the emitted light is linear polarized in the plane of the disk motion. This polarization direction can be changed by scattering in the accretion disk or the light could be blocked by a corona. The coronal influence depends on the temperature, the geometrical thickness, and the optical depth of the corona. The scattering effects

in the disk depend on the optical depth of the disk. A large optical depth can explain polarization direction lying in the rotation plane of the disk, while a small optical depth would explain polarization along the axis of rotation [22]. Furthermore, the polarization depends on the kinematics of the system. A Newtonian accretion disk is expected to emit light with a high degree of polarization. That is in contrast to the prediction of weak polarization for a disk where general relativistic effects come into play [23]. The next process affects photons in the lower keV range. They can be gravitationally bend around the BH and scatter again in the disk. This effect causes polarization perpendicular to the rotation axis for low energies. However, larger energies cause polarization parallel to the rotation axis of the system [24][25].

Since direct imaging of a BHB is hardly possible, spectral, temporal, and polarimetric features are the only way to gain information about the structure of the astrophysical object. By measuring the degree and the plane of polarization it is possible to draw conclusions on several parameters of the source object. The data of different energy ranges provide complementary information about the system. Several measurement have been done so far but not for all energy ranges. In general, it is important to have continuous measurements due to the strong variability of the emitted spectrum (see figure 2.1). To understand the different emission states and transition mechanisms it is necessary to have a continuous observation.

ComPol will simultaneously operate as a spectrometer and a polarimeter. It will observe Cygnus X-1 in the energy range between 20 keV and 2 MeV. Due to the strongly decreasing flux for energies > 400 keV, ComPol's sensitivity for the polarization of Cygnus X-1 will be limited to the energy range < 400 keV. The Compton telescope IBIS (see section 1.3) determined an upper limit of 20% polarization in the energy range from 250 keV to 400 keV and a high degree of polarization ($\sim 70\%$) for the energies from 400 keV to 2 MeV (see figure 2.5) [26]. So far, hardly any polarization measurements have been performed in the range from 20 keV to 200 keV. Therefore, ComPol can help to understand the emission mechanisms of hard X-rays and give insights to the processes happening in the regions closest to the black hole. The additional spectral measurement up to 2 MeV provides a temporal tracking of spectral variations and can contribute to understanding of the state transitions and of the hard photon tail (> 400 keV).

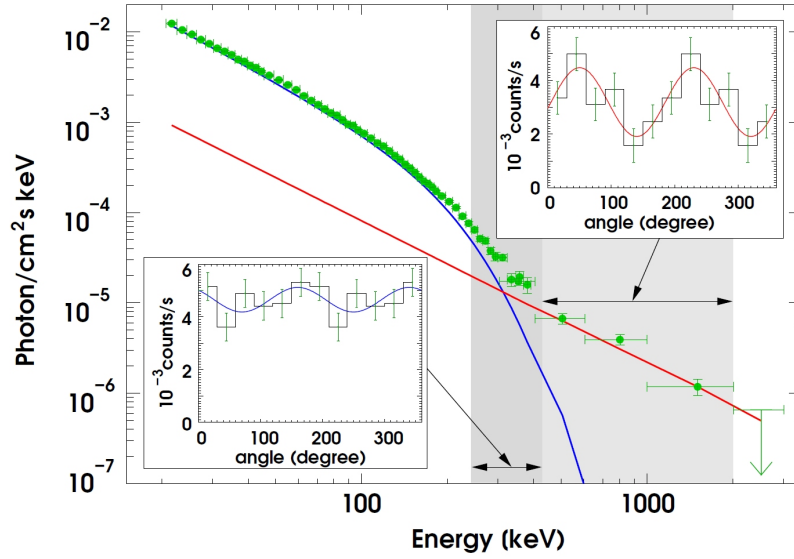


Figure 2.5: The plot displays measurement results of the IBIS/INTEGRAL mission. The spectrum shows two different components, a high energy part (blue) and a hard X-ray tail (red). The polarization was determined for two different energy ranges. A weak polarization ($0\% < P \lesssim 20\%$) was calculated for the energy range from 250 keV to 400 keV. Whereas, the X-rays from 400 keV to 2 MeV showed a strong polarization of $\sim 70\%$ [26]. The figure is taken from [27].

2.2 CubeSats

Conventional space missions became more and more complex, expensive, and time consuming. Over the past 20 years, CubeSats (Cube Satellites) came up as a cheap, fast, and easy-to-use alternative. They are miniaturized satellites built out of standardized units. Each unit has a size of $10 \times 10 \times 11.35 \text{ cm}^3$ and a maximum weight of 1.3 kg [28]. Up to 24 units can be stacked together to obtain larger satellites. Due to the strong size and weight limitations, CubeSats have to be built very minimalistic. The duration of typical CubeSat missions are a few years. Without heavy shielding, the electronics are exposed to a lot of cosmic rays and electromagnetic radiation. This is a major reason for the short half-life of CubeSat missions compared to larger satellites.

At this point, it is worth noting that the goal of ComPol is to achieve a scientific result, since CubeSats are often used only to test systems for larger projects.

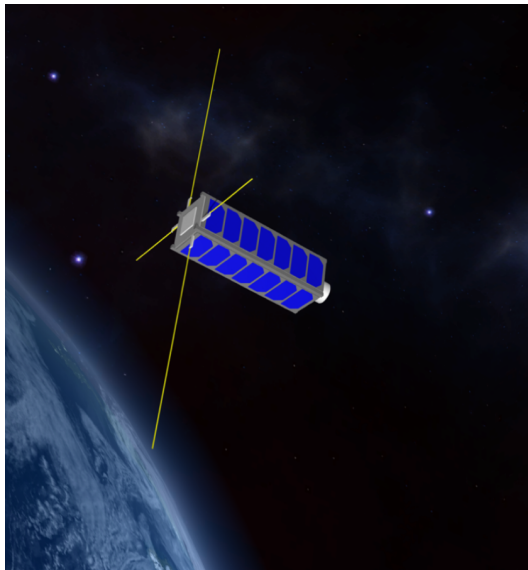


Figure 2.6: Visualization of the ComPol CubeSat in space [29]. The detector system fills approximately one third of the satellite and is placed in the end pointing to the lower right. The white tube protruding from the cuboid is the collimator in front of the detector system. The sides are covered with solar cells. The yellow lines represent the unfolded antenna system.

2.3 Set-up

The ComPol CubeSat is made up of three units. The outer dimensions of the basic structure are $10 \times 10 \times 34 \text{ cm}^3$. One of the units will be occupied by the detector system of ComPol. The other units will be needed for batteries, a board computer, a magnetorquer board and reaction wheels for alignment of the satellite, a transmitter unit, etc. The collimator in front of the detector system will protrude from the front end. In operation mode, the antenna system at the other end of the CubeSat will be unfolded. It also exceeds the dimensions of the basic structure (see visualization in figure 2.6).

The detector system of ComPol is build like the set-up introduced in chapter 1.2.1, two different detectors are placed behind another. The upper layer is a **Silicon Drift Detector (SDD)** and the lower detector is a CeBr_3 scintillator. The SDD was originally developed for the upcoming extension of the KATRIN experiment for sterile neutrino search (TRISTAN project [30]) at the **Karlsruhe Institute of Technology (KIT)** in Karlsruhe, Germany.

In front of the SDD is a lead collimator to allow the detector to only focus on one

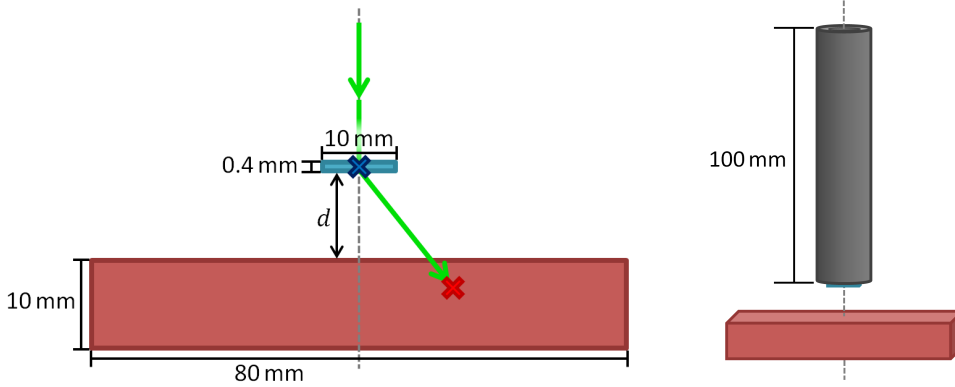


Figure 2.7: Detector set-up for the ComPol project. In blue the TRISTAN SDD and in red the CeBr_3 scintillator. Both detectors have approximately a quadratic base. The indications of size are preliminary.

Left: Detector set-up with an exemplary X-ray event. It shows a Compton scattering (blue cross) in the SDD and a photoelectric absorption (red cross) in the scintillator.

Right: Detector set-up with lead collimator in front.

source. The left part of figure 2.7 shows the detector set-up and the same set-up with the collimator on the right side. The indicated dimensions are preliminary. However following limitations and constraints have to be considered. The SDD thickness will not change due to the production conditions. The width of the SDD is limited to the inner collimator diameter. The width of the scintillator is limited to 8 cm because of the CubeSat dimensions. The most interesting parameters which have to be optimized for the specific use of ComPol are the thickness of the scintillator and the distance d between the two detectors. A thicker scintillator has a higher absorption efficiency. However, it would reduce the energy and position resolution. For the detector distance d , it is necessary to balance between angular resolution and total number of useful events. Due to the limited position resolution of the detectors, the uncertainty on the scatter angles increases with decreasing distance d . On the other hand, the solid angle covered by the scintillator is reduced by increasing the distance d . This causes a reduction of the total number of photons which are Compton scattered in the SDD and absorbed in the CeBr_3 . The polarization signal is reduced simultaneously due to the dependence of the Compton cross section on the scatter angle θ (compare figure 1.8). The dimensions of the collimator tube for the best background reduction have to be optimized too. The inner radius is planned to be approximately 7.5 mm and the thickness of the tube wall between 1 mm and 10 mm.

2.3.1 TRISTAN detector

TRitium **I**vetigations of **S**terile to **A**ctive **N**eutrino mixing (**TRISTAN**) is the name of an upcoming project within the KATRIN collaboration in Karlsruhe, Germany. The laboratory-based experiment aims at searching for sterile neutrinos. It will be an upgrade of the currently running **K**Arlsruhe **T**Ritium **N**eutrino **E**xperiment (**KATRIN**) which holds the best limit of 1.1 eV on the electron neutrino mass via direct measurement [31]. In both experiment phases of KATRIN, electrons from tritium decays are measured, to draw conclusions on the (sterile) neutrino mass. For detailed informations about the KATRIN experiment and its set-up, [32] is recommended and [33, 30] for further informations about the TRISTAN project.

The electron detector for the TRISTAN experiment has to handle very high count rates and needs a precise energy measurement (< 300 eV FWHM at 20 keV). The ideal technology to combine high energy resolution and high rates is the **S**ilicon **D**rift **D**etector (**SDD**). Its design is optimized to handle rates up to 100 kcps and provide a very good energy resolution (140 eV FWHM at 5.9 keV [33], for more details see section 2.3.3). This precise energy measurement predestines the SDD technology for the ComPol experiment. For an efficient background exclusion (see chapter 3.5) it is required to accurately measure the energy deposition during Compton scattering. Another reason for using this detector type is the relatively small atomic number Z of silicon ($Z_{\text{Si}} = 14$). As shown in section 1.1 the cross section for Compton scattering has no dependence on Z . But the cross section for photoelectric absorption scales with Z^5 . For a successful event reconstruction it is necessary to have a Compton scattering with subsequent photoelectric absorption of the photon. By reducing the number of photons absorbed in the first detector layer, the number of events having a Compton interaction in the first detector layer increases. Therefore it is advantageous to use a detector material with a small atomic number. A detailed description of these Compton events and their reconstruction can be found in section 1.2.1.

Silicon drift detectors

A silicon drift detector is a special type of a semi-conductor detector. The best way to understand its characteristics, is by comparing the SDD technology with the classical PIN diode. Both instrument types are made for the detection of ionizing radiation, e.g. photons, electrons. A **P**IN diode is made up of a **P**ositive doped (p-doped), a **N**egative doped (n-doped), and an undoped **I**ntrinsic semiconductor. The intrinsic region is placed between the two charge doped regions to increase the size of the depletion zone (first part of figure 2.9). In general a depletion zone is build out at the boarder of a positively and a negatively doped region. The electron hole pairs recombine and the remaining atoms generate an electric field inside the depletion zone, as it is shown in figure 2.8. This is called a p-n junction. The depletion zone

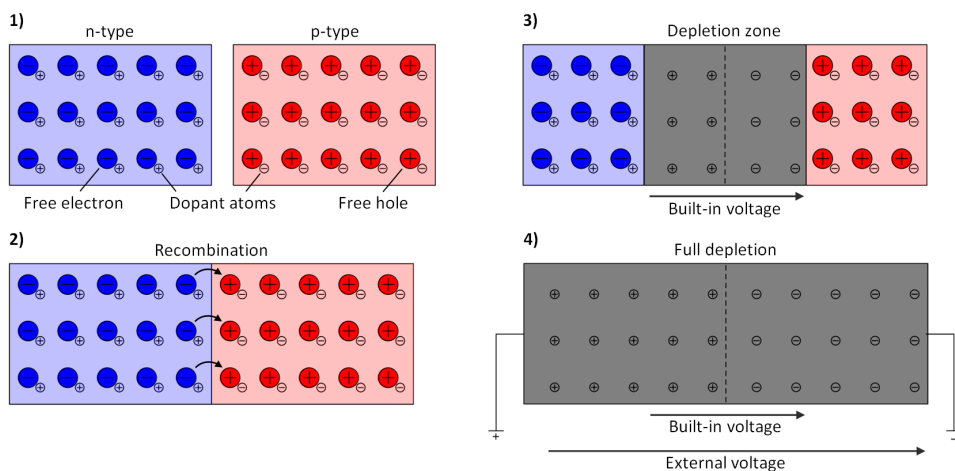


Figure 2.8: Schematic description of a p-n junction (adapted from [34]).

1) Differently doped semiconductors: n-doped (blue), p-doped (red). In the n-type region are free electrons and their remaining positively charged atoms. It is the other way round in the p-type region, free holes and their negatively charged remaining atoms. **2)** The differently doped materials are connected. The electrons recombine with the holes of the p-doped region. **3)** The created region without free charge carriers is called depletion zone. An internal voltage is built up, which prevents the recombination of further electron hole pairs. **4)** An external voltage reinforces the effect. The depletion zone is extended over the complete material.

can be increased up to a certain limit by applying an external voltage in the direction of the internal electric field. The size of the depletion zone is directly correlated with the detection efficiency because it is the sensitive volume of the diode. Interactions of the incident radiation in the depletion zone create electron hole pairs. The electrons are attracted by the anode, where they are detected with a readout system. The number of created electrons and thus the intensity of the measured signal scales with the energy deposited in the detector volume.

In SDDs, the principle of sideways depletion is applied. This is shown in the second part of figure 2.9. With additional p-doped regions on the bottom side, a much smaller anode is enough to reach the same level of depletion. In the third part of figure 2.9 the external voltage is increased to obtain a completely depleted detector volume. Free electrons that are created in the outer part of the detector will not reach the anode, since they move mostly due to diffusion through the flat potential minimum. This problem is fixed in the last part of the figure. The bottom p-doped region is divided into several rings around the anode, called drift rings. These rings

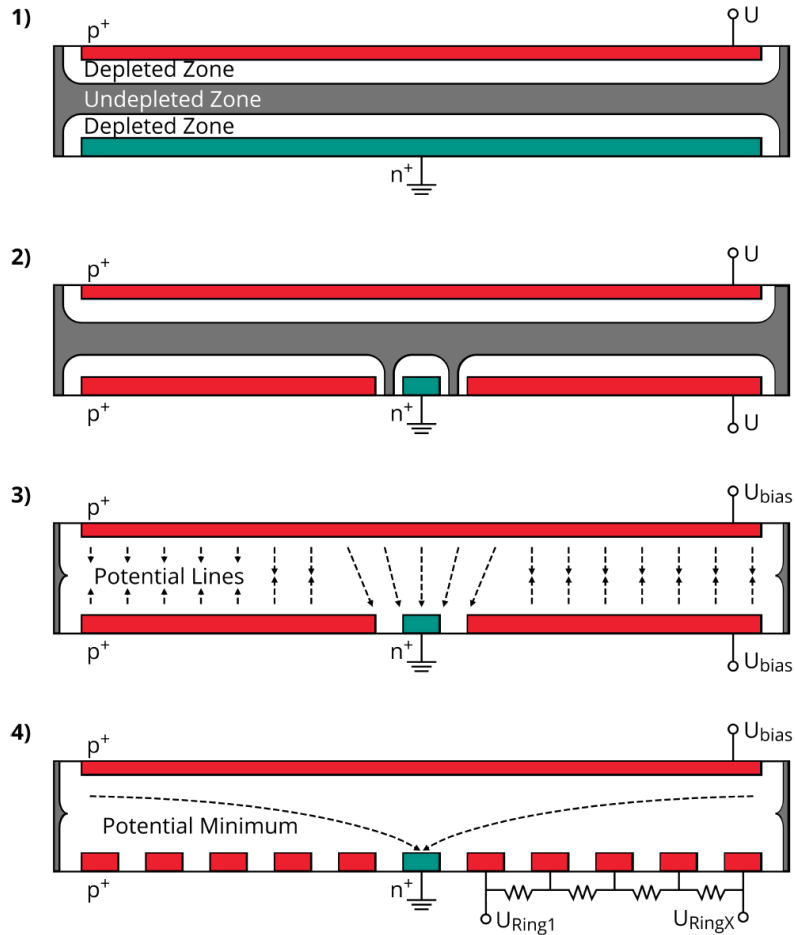


Figure 2.9: Schematic evolution of a PIN diode to an SDD. The figure is adapted from [34].

1) Cross-section of a classical PIN diode consisting of a p-doped cathode, an n-doped anode, and an undoped intrinsic semiconductor in between. 2) The outer anode regions are replaced by additional p-doped regions. 3) The external voltage is increased to deplete the complete detector volume. 4) The p-doped area is divided into several rings around the anode. These rings are supplied with voltages rising to the outside (becoming more negative) to provide an electric field guiding all free electrons to the anode.

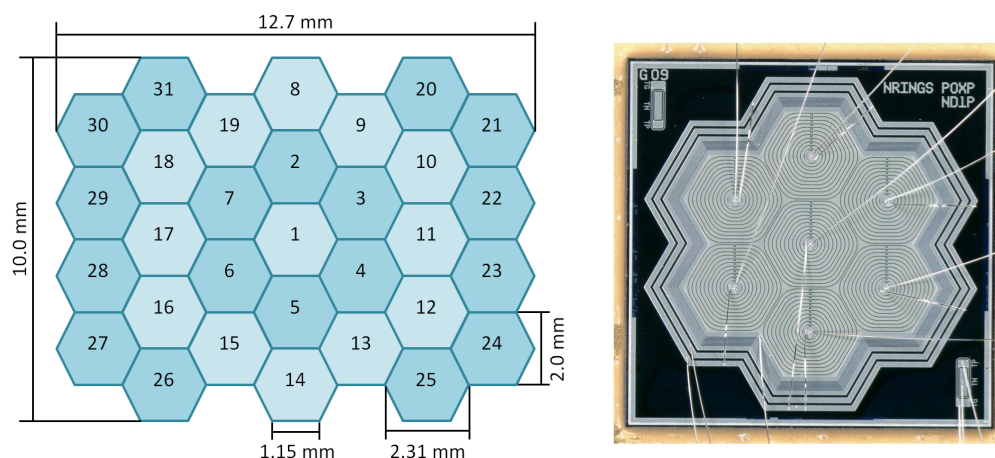


Figure 2.10: Module design and prototype of the silicon drift detector.

Left: Preliminary geometry of the SDD for the ComPol experiment. The module consists of 31 hexagonal pixels with a size of 2 mm.

Right: Seven pixel prototype of the TRISTAN SDD. The anode is located in the center of each pixel and surrounded by the drift rings. The pixels of the shown prototype have the same dimensions like the ones in the sketch on the left. Two bonding wires are attached to each pixel, one for the anode and one for the innermost drift ring. The outermost drift rings are connected so that individual bonding wires for each pixel are not required.

are supplied with voltages rising to the outside (becoming more negative). This creates an electric field that guides the free electrons to the anode.

The small anode area is the overall advantage of the SDD technology compared to classical PIN diodes. The noise is strongly reduced due to this low capacitance anode design which leads to a much better energy resolution.

SDD module for the ComPol project

The SDD module for the ComPol experiment will be made up of several hexagonal pixels. The preliminary module design is shown in the left part of figure 2.10. It consists of 31 pixels. Each pixel has a size of 2 mm. The overall dimensions of the module are $10 \times 12.7 \text{ mm}^2$. In the rest of this thesis the dimensions of the SDD are approximated by a $10 \times 10 \text{ mm}^2$ quadratic shape.

At the moment, the TRISTAN collaboration invests large effort into characterization of the TRISTAN SDD. A seven-pixel prototype used for this purpose is shown in the right part of figure 2.10.

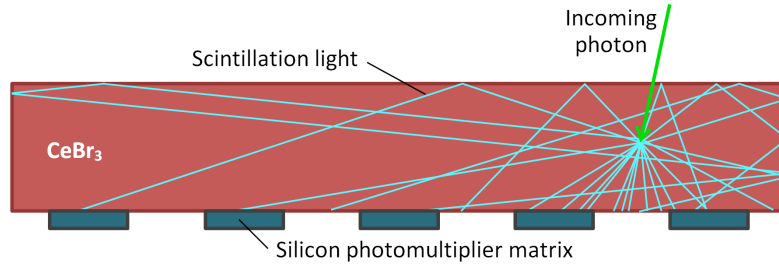


Figure 2.11: Sketch of the working principle of the CeBr_3 calorimeter. The incoming photon (green) is absorbed by the crystal. The crystal emits scintillation light (blue) at the interaction point. The light distribution is measured by the photomultiplier matrix. The interaction point can be reconstructed from the measured light distribution.

2.3.2 CeBr_3 calorimeter

The requirements for the calorimeter are a good absorption efficiency for X-rays, a position resolution of the same order of magnitude as the first detector layer, and the ability to measure the energy of the absorbed photons. A detector material which fulfills these requirements is cerium(III) bromide (CeBr_3). It is an inorganic scintillating crystal. Scintillation light is created when ionizing radiation interacts in the detector volume. The wavelength of maximum emission for CeBr_3 is at 380 nm and the light yield per deposited energy is about 68 photons per keV [35]. This scintillation light can be measured by photomultipliers placed on the material surface.

The CeBr_3 module of the ComPol project has a size of $8 \times 8 \times 1 \text{ cm}^3$. It is read out by **Silicon Photomultipliers (SiPM)**. The deposited energy is determined by evaluation of the total light yield and the position of the interaction point is determined by analyzing the light distribution measured by the SiPMs. Artificial neural networks are used to solve this problem. After training with data from simulations, the interaction point can be determined with an accuracy in the order of a few millimeter (see section 2.3.3). A detailed description and characterization of this technique is explained in [36]. The sketch in figure 2.11 illustrates this process. The light distribution measured by the SiPM array depends on the position of the interaction point.

2.3.3 Detector resolutions and energy limits

This section give an overview of the energy resolution, the energy threshold, and the position resolution for both detectors.

- **Energy resolution**

Both detectors have an energy dependent energy resolution. For the SDD it is dominated by the Fano noise:

$$\sigma_{\text{Fano}} = \sqrt{F \cdot \omega \cdot E}, \quad (2.1)$$

with the Fano factor F and ω as the energy necessary to create an electron hole pair in silicon. Both parameters are temperature dependent. The outer surfaces of a satellite are exposed to very strong temperature variations (-270°C to 80°C). The impact for the internal space is much lower. The temperature is expected to be between -20 and $+20^\circ\text{C}$ [37]. For this temperature range the Fano factor is $F \approx 0.13$ and the energy to create an electron hole pair $\omega \approx 3.64$ eV see [38].

The noise contribution $\sigma_{\text{el}} \approx 35.7$ eV of the detector electronics and the read-out chain is rather small compared to the Fano noise [39]. The total energy resolution for the SDD is given as:

$$\sigma_{\text{E,SDD}} = \sqrt{F \cdot \omega \cdot E + \sigma_{\text{el}}^2} \quad (2.2)$$

The visual comparison between the Fano limit σ_{Fano} and the total energy resolution of the SDD is shown in the left part of figure 2.12.

The energy resolution $\sigma_{\text{E,Cal}}$ for the CeBr_3 calorimeter was measured by Gos-tojić [36]. The values for $\sigma_{\text{E,Cal}}$ were determined by measuring the FWHM of several X-ray and γ -ray lines for different radioactive sources, see table 2.1. An interpolation of these values is presented in the right part of figure 2.12. The interpolation is used for the sensitivity study in chapter 3.

- **Energy limits**

The lower detector thresholds for the energy measurements are:

$$E_{\text{min,SDD}} = 1 \text{ keV} \quad \text{and} \quad E_{\text{min,Cal}} = 10 \text{ keV}.$$

The cross section for photon absorption and therefore the stopping efficiency decreases with increasing energy. At energies higher than 7 keV, photons start to pass the 400 μm thick silicon detector. The 1 cm thick CeBr_3 detector starts to become transparent at about 90 keV. These values are no hard upper energy limits. They just indicate the energy from where on the stopping efficiency slowly decreases.

Table 2.1: Measured energy resolution $\sigma_{E,Cal}$ for the calorimeter. The measurement was done for several energies of different radioactive sources [36].

Line origin	Line energy (keV)	$\sigma_{E,Cal}$ (keV)
Ag K_α X-ray	22.1	3.1
Cs K_α X-ray	30.9	3.5
γ ^{241}Am	59.5	4.5
γ ^{133}Ba	80.9	5.0
γ ^{133}Ba	276.4	9.4
γ ^{133}Ba	302.9	9.4
γ ^{133}Ba	356.0	10.1
γ ^{133}Ba	383.8	12.2
γ ^{137}Cs	661.7	13.5
γ ^{60}Co	1173.2	23.9
γ ^{60}Co	1332.5	27.1

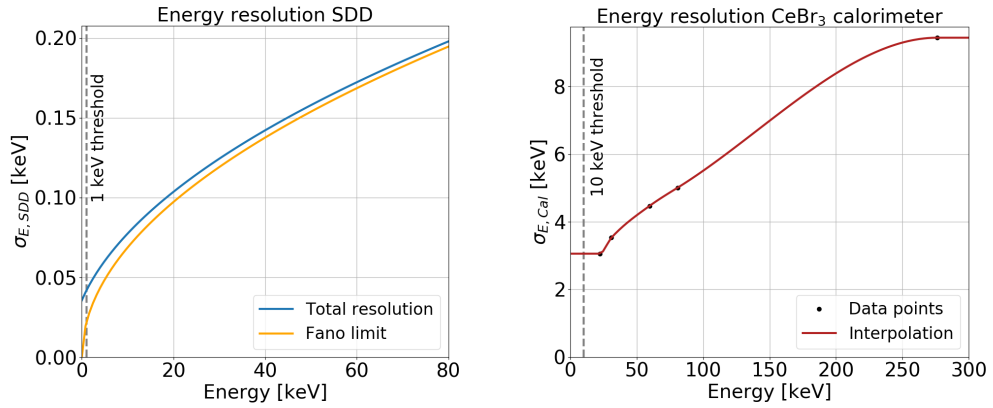


Figure 2.12: Energy resolutions of the silicon drift detector and the CeBr₃ calorimeter. The dashed lines show the lower energy thresholds.

Left: Comparison of the total energy resolution of the silicon drift detector with the Fano limit.

Right: The energy resolution of the CeBr₃ calorimeter was measured for discrete energies (see [36]). The displayed interpolation is used in chapter 3.

- **Position resolution**

The position resolution of the SDD is determined by the pixel size. The pixels are hexagonally shaped. Each edge of these hexagons has a length of 1.15 mm. The total pixel size (distance between two opposite edges) is therefore 2 mm, which is a good estimate of the position resolution in the conventional sense. The thickness of the pixels is 400 μm . The arrangement of the pixels is shown in figure 2.10.

The calorimeter is not segmented into pixels. Only the silicon photomultipliers are pixelized. The position of an interaction in the calorimeter is reconstructed from the light distribution on the SiPMs (illustration in figure 2.11). It is distinguished between the position resolution σ_{\parallel} parallel to the detector plane and a position resolution σ_{\perp} in the direction of the smallest detector dimension. The resulting position resolutions for the scintillator used in ComPol are as follows:

$$\sigma_{\parallel, \text{Cal}} = 2.5 \text{ mm} \quad \text{and} \quad \sigma_{\perp, \text{Cal}} = 2.2 \text{ mm}.$$

A detailed description of the reconstruction with an artificial neural network and the resulting overall detector performance of the CeBr_3 calorimeter is described by Gostojić [36].

2.4 Conclusion

The CubeSat mission ComPol aims at measuring the polarization and the spectrum of the black hole binary system Cygnus X-1 in the hard X-ray range. The scientific goal is to improve the physical model of Cygnus X-1. By measuring the polarization and the spectrum, it is possible to draw conclusions on the emission region. For hard X-rays this is predicted to be very close to the black hole horizon.

ComPol's detector set-up consists of a **Silicon Drift Detector (SDD)** and a CeBr_3 calorimeter. The SDD acts as a scatterer for the incoming photons, which are subsequently absorbed in the calorimeter. The excellent performance of the specific SDD allows to accurately measure the energy deposits of these Compton events.

To make a meaningful statement on the polarization, it is necessary to collect at least several hundred Compton events. The required number increases with additional background. However, ComPol's detector area is strongly limited due to the size restrictions for CubeSat experiments. Therefore, it has to be proven, that the system can collect enough data to be sensitive for the expected degree of polarization of Cygnus X-1.

Chapter 3

Sensitivity study

Designing the detector system for a CubeSat is a challenging task. The different components have to fulfill stringent space and weight limitations. Moreover, they must be within the limits of the CubeSat's power supply and have to withstand strong temperature variations. To take full advantage of these limited possibilities, it is necessary to plan carefully. Usually, buying the hardware in different detector configurations is expensive, therefore a simulation based design study is a convenient alternative. Furthermore, satellites are exposed to a lot of cosmic rays and electromagnetic radiation from space. This is especially critical for CubeSat missions because the strict weight specifications do not allow thick shielding. Thus, it is also crucial to make detailed background studies to obtain a meaningful sensitivity for the desired observable.

This chapter describes the performed study for the ComPol project. Sections 3.1 and 3.2 introduce the used Monte Carlo tool Geant4 and the general simulation settings. The subsequent sensitivity study is split into an analysis part for the signal simulation (section 3.4) and an analysis part for the background study (section 3.5). Finally, section 3.6 concludes with the estimation of ComPol's sensitivity on the polarization of Cygnus X-1 in the energy range from 10 keV to 300 keV.

3.1 Introduction to Geant4

Geant4 is a tool kit widely-used in particle physics. It is a Monte Carlo tool for simulating particle interactions with matter [40]. It is used for a variety of applications in particle physics, nuclear physics, astrophysics, medical physics, and other fields. Geant4 is often used for detector or accelerator design as well as for verification of physical models and measurement data. The C++ based software has been developed by a world-wide collaboration of scientists and software engineers. Its origin is in the research center CERN in Geneva. This large development team and a high degree of customization make Geant4 one of the most powerful particle simulation tools available.

The individual geometry of the set-up is chosen by the user. This includes the detector design, the particle source, and surrounding materials. Geant4 accesses

a data base with properties of all chemical elements, their weight, electron configuration, binding energies, cross sections, etc. The user constructs volumes of the desired shape and assigns a material to each volume. It is also possible to create custom compound materials and to define electromagnetic fields. Therefore, it is easily possible to implement any user-specific geometry. Geant4 is also very flexible in the selection of particles to be simulated. It is possible to simulate all particles of the standard model and even user-defined particle types. Additionally, Geant4 is designed to freely choose the necessary interaction types, disable single processes or even define new ones. The implemented physics are applicable from 250 eV up to several PeV (10^{15} eV). For simplification, the user can choose between major groups of physical processes:

- Particle decay processes
- Electromagnetic interactions
- Solid state physics
- Hadronic interactions
- Photoleptonic interactions

Geant4 simulates each initial particle and the secondary particles produced during an event. Each event starts with the creation of an initial particle in the source and ends after tracking all particles, until they are absorbed or leave the region of interest. The number of events is defined by the user. With Geant4 it is possible to store the informations about all single interactions, including each position, time, interaction type, deposited energy, particle type etc.

Geant4 is used in this thesis to simulate the set-up of the ComPol project. Firstly, section 3.4 focuses on the polarization signal from Cygnus X-1. Secondly, section 3.5 is devoted to the influence of the background in a low Earth orbit (~ 500 km). The software version used for this thesis is Geant4 10.4.2.

3.2 Simulation settings

To obtain consistent results, the same physics list and geometry is used for all simulations. The parameters of the particle source are different for the signal and the background simulation. The following sections describe the used settings:

Physics list

The so-called physics list defines the particles and the physical processes which are considered during the simulation. The used physics list is generated by the

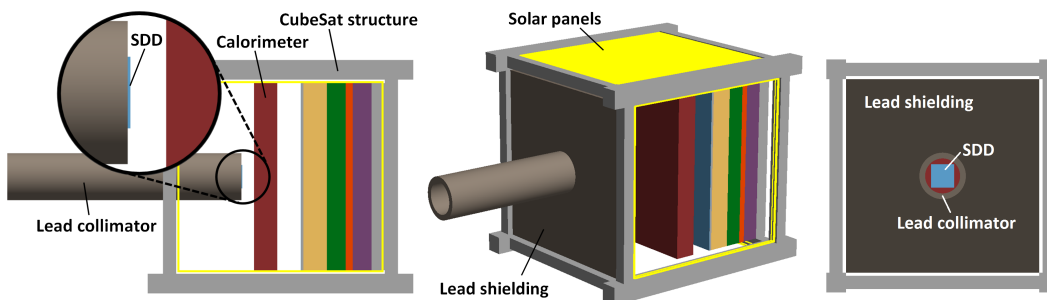


Figure 3.1: Visualization of the set-up used for the simulations. The set-up is strongly simplified, from three CubeSat units to only one (dimensions of one unit: $10 \times 10 \times 11.35 \text{ cm}^3$). This is done because the final satellite design is not completely determined yet and to reduce the simulation time. The set-up consists of the Silicon Drift Detector (SDD), the CeBr_3 calorimeter, a lead collimator, a lead shielding around the collimator covering the front side of the Cube, the basic CubeSat structure, solar panels on all four sides (indicated by yellow lines), and a block of different material layers behind the detector system. These material layers account for the material distribution in the final CubeSat. A detailed description of the geometry with all dimensions and materials can be found in the appendix A.

Left: Side view of the set-up with a zoom to the SDD. The solar panels are transparent, to show the internal structure.

Center: 3D perspective, with a non-transparent solar panel on the top side.

Right: View from the front. SDD and collimator are aligned on the longitudinal axis of the CubeSat.

`G4EmLivermorePolarizedPhysics` constructor. This is a predefined physics list from Geant4 for the low energy range (250 eV to 100 GeV). It contains electromagnetic interactions, including polarized gamma models.

Geometry

The detector system is implemented as it is shown in the left part of figure 2.7. The distance d between the detectors is set to 5 mm. The collimator in front of the detector system sits on the plane of the entrance window of the SDD. The collimator dimensions are implemented according to table A.3 in the appendix. From these values, the resulting wall thickness is 2.5 mm. The inner radius is chosen that the SDD is not covered by the collimator wall.

Especially for the background simulation, it is important to implement the basic

structure and material distribution of the CubeSat itself. It acts like a shielding and can produce secondary radiation. A visualization of the complete simulation set-up is shown in figure 3.1. A detailed description of the geometry with all indications of size and materials can be found in the appendix A.

Particle source

Three different particle sources are used for the simulations in this thesis:

1. **Monoenergetic beam**

The source emits 100 % polarized photons in a monoenergetic pencil beam. The beam points on the center of the silicon detector. The direction is aligned with the longitudinal axis of the CubeSat. This source was used to study different interaction types in the detector system and to investigate energy dependent effects.

2. **Realistic Cygnus X-1**

The whole silicon detector is illuminated with a quadratic ($10 \times 10 \text{ mm}^2$), 100 % polarized photon beam. Its energy distribution is modeled according to the actual X-ray spectrum of Cygnus X-1 in the low hard state [15] (see figure 3.2). The states of Cygnus X-1 are explained in section 2.1. The simulated energy range is between 10 keV and 300 keV.

3. **Background source**

The background particles originate from a spherical surface around the detector set-up. The initial direction is according to the cosine emission law of Geant4, to generate isotropic radiation. The energy spectra (see figure 3.3) correspond to measured background spectra in a low Earth orbit (550 km) [41]. The following particle types are used for the simulation: Photons, electrons, positrons, protons, and alpha particles.

The applied normalizations for the three source types are described in the appendix B.

3.3 Detector response

The implementation of the detector response allows a more realistic description of the instrument's performance. Both, the silicon drift detector and the CeBr_3 scintillator have a limited energy and position resolution and a lower energy threshold. The respective values are summarized in chapter 2.3.3. The detector response is applied to the data after the simulation. This makes it possible to investigate the impact of the different parameters on the final result.

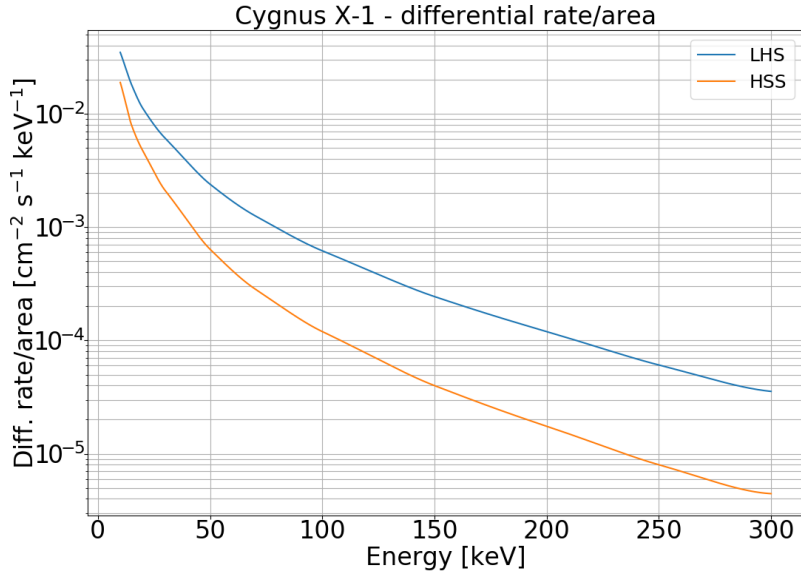


Figure 3.2: Energy spectrum from 10 keV to 300 keV of Cygnus X-1 in the Low Hard State (LHS) and the High Soft State (HSS), see section 2.1 for the state description. The LHS spectrum is used for the simulation of the realistic Cygnus X-1 particle source. The data is taken from [15].

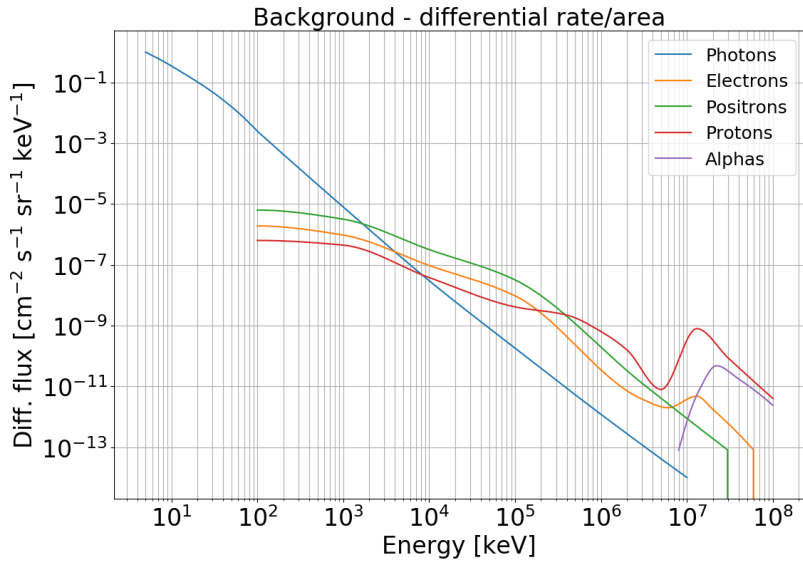


Figure 3.3: Background spectra in a low Earth orbit (550 km) for photons, electrons, positrons, protons, and alpha particles. These spectra are used for the background particle source. The data is taken from [41].

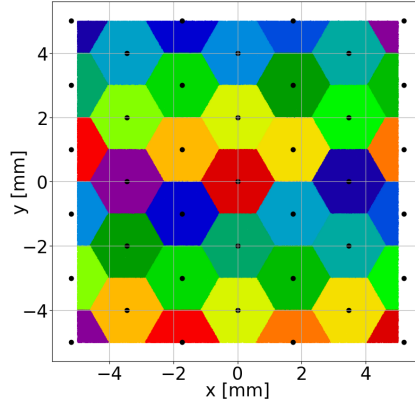


Figure 3.4: Implemented pixel map of the SDD. The black dots indicate the center points of the pixels. The actual detector will be a bit larger than $10 \times 10 \text{ mm}^2$. To account for that, also the outer areas are treated as pixels.

Implementation of the energy resolution

The energy resolutions of the two detectors are implemented as Gaussian uncertainties. For each detector, the width of the Gaussian is energy dependent. The total energy deposit for each event is shifted by a random value drawn according to this Gaussian distribution.

Implementation of the energy thresholds

If the total energy deposit per event is lower than the energy threshold of the respective detector, its value is set to zero.

Implementation of the position resolution

The positions of all single interactions in each detector are weighted by the respective energy deposits. This is done for all events to obtain the weighted average interaction positions. The final resolution is modeled differently for the SDD and the calorimeter.

For the SDD, each average interaction point is assigned to a pixel and shifted to the center of the respective pixel. The used pixel map is shown in figure 3.4. Charge sharing between two pixels is not considered.

The interaction point in an actual CeBr_3 scintillator is reconstructed from the distribution of the scintillation light. The resulting position distribution is not discrete. However, the simulation in this work does not include the production of the scintillation light. Therefore, it is assumed that the position resolution is Gaussian. Each average position is treated accordingly. The outer dimensions of the calorimeter are considered as limits for the maximum displacement.

3.4 Signal simulation

ComPol aims at measuring the spectrum and the polarization of Cygnus X-1. The sensitivity study in this thesis refers to the sensitivity on the degree of polarization. The performance for spectroscopy is not discussed. The following section deals with the signal simulation (events coming from Cygnus X-1) and with the subsequent analysis of the simulation data.

To understand the observed signal of polarized X-rays, the study includes two steps. The first step is the simulation of a 100% polarized, monoenergetic X-ray beam pointing on the two-layer detector set-up described in section 3.2. This simulation allows to investigate the different interactions in the two detectors and the energy-dependent detection efficiency for polarization. The second step is the same simulation but with a realistic energy spectrum of Cygnus X-1. This simulation is used to determine a realistic estimation of the polarization sensitivity for ComPol.

As a first step of the study, it is helpful to classify the large variety of different processes in the detector system. The most interesting events with regard to polarimetry are:

Compton events

The incoming X-rays of these events undergo Compton scattering in the silicon detector and subsequently photoelectric absorption in the calorimeter (Visualization in center part of figure 3.9).

The detector output for these events carries information on the polarization dependence of the Compton scattering. Most of the other events cannot be used for polarimetry. The following section 3.4.1 gives an overview of all possible events in the SDD and section 3.4.2 of the events in the calorimeter. Subsequently, the rates of the interesting processes are discussed in section 3.4.3. All Monte Carlo data presented in these three sections are based on simulations with monoenergetic photon beams. Furthermore, section 3.4.4 is devoted to the event selection for the situation with the realistic Cygnus X-1 source. Finally, section 3.4.5 describes the polarization analysis.

3.4.1 Interaction types in the SDD

The silicon detector is intended to serve as the scatterer for the incoming X-rays. The favored events are the ones with one single Compton scattering inside the SDD, shown in the left part of figure 3.5. Such an event potentially ends up as a Compton event, as long as the outgoing X-ray is scattered towards the calorimeter. In principle, events with more than one Compton scattering in the SDD (central part of figure 3.5) can be also used for the polarization analysis. For a correct reconstruction, these

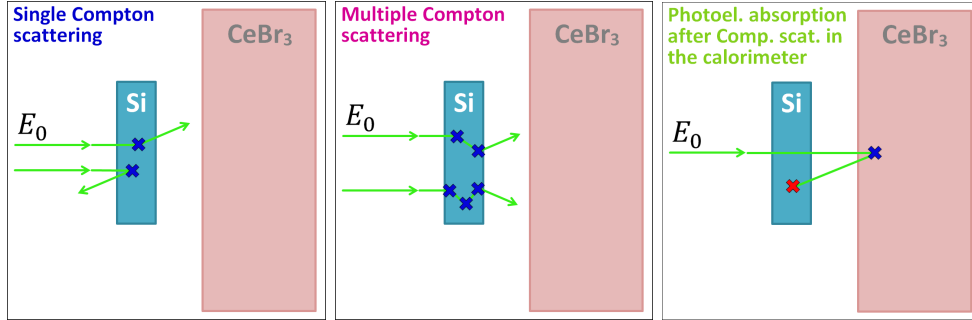


Figure 3.5: Visualization of events in the SDD for the first stage of event classification. These events are potentially interesting for polarimetry.

Left: The initial photon undergoes single Compton scattering (blue cross) in the silicon detector and no other interaction takes place inside the SDD. These are possible Compton events, depending on the further photon path.

Center: The initial photon undergoes more than one Compton scattering in the silicon volume and no other interaction takes place inside the SDD.

Right: The initial photon passes the silicon detector without interaction. Afterwards it undergoes one single Compton scattering in the CeBr₃ calorimeter. From there it returns to the SDD, where it is completely absorbed via photoelectric effect (red cross). These events are called inverted Compton events.

Compton scatterings have to take place in two different pixels of the SDD. Even though improbable for such a thin detector, these events are still mentioned here as potentially useful for polarimetry. Inverted Compton events form the last potentially useful event class. The initial photon of these events scatters in the CeBr₃ calorimeter and is absorbed in the silicon detector (right part of figure 3.5).

Event types for the silicon detector, which cannot be used in the polarization analysis, are shown in figure 3.6. An example for such an event is the absorption of the initial photon in the SDD so that it does not even pass to the calorimeter (left part of figure 3.6). This category includes events with escaping secondary particles. Another undesired event class contains events with Rayleigh scattering (central part of figure 3.6). Events with a Compton scattering before or after the Rayleigh scattering are also not useful. The direction of the Compton scattered photon depends on the initial polarization vector. This information on the polarization is lost with an additional deflection by Rayleigh scattering. The last category of unintended events includes all events with secondary particles returning from the calorimeter (right part of figure 3.6).

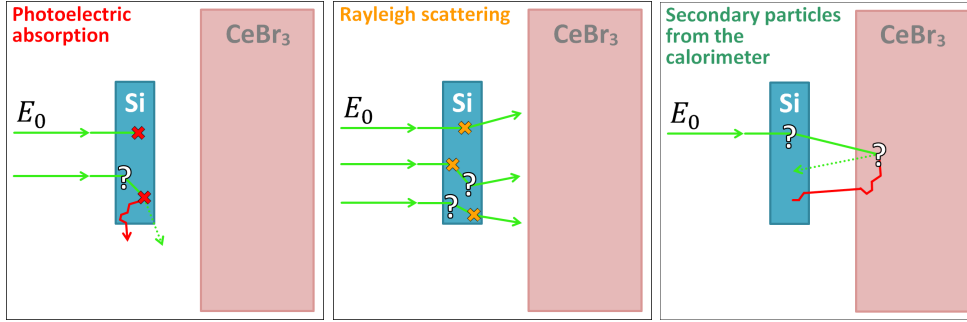


Figure 3.6: Visualization of events in the SDD for the second stage of event classification. These events are not useful for polarimetry.

Left: The initial photon is absorbed via photoelectric effect in the SDD. It does not pass to the calorimeter. This category includes events with other interactions of the initial photon in the silicon before it is absorbed. Events with escaping secondary particles are also included in this category.

Center: The initial photon undergoes Rayleigh scattering (orange cross) in the silicon detector and leaves the detector volume again. Events with other interactions before or after the Rayleigh scattering are included.

Right: This category contains all events with secondary particles returning to the silicon detector from the calorimeter.

Energy spectrum of the silicon detector

Figure 3.7 shows a spectrum of the silicon detector from a simulation with a monoenergetic 60 keV photon beam. It shows the total energy deposit per event for 10^6 simulated events. The complete spectrum is illustrated as a gray area and all mentioned event classes are additionally displayed in color. Most of the following spectral features are energy dependent. The appendix C.1 contains spectra for different initial energies (30 keV, 100 keV, 150 keV, and 300 keV) for comparison.

- **Total energy spectrum**

The gray area in figure 3.7 has a large peak at 0 keV caused by X-rays passing the SDD without any interaction. This feature is related to the absorption efficiency of the SDD which decreases with increasing photon energy.

- **Single Compton scattering**

The single Compton distribution strongly decreases for energies larger than the so called Compton edge. It is defined as the maximum transferable energy E_{CE} for Compton scattering. Equation 3.1, derived from equation 1.1, defines

the energy of the Compton edge.

$$E_{\text{CE}} = \frac{E}{1 + \frac{m_e c^2}{2E}} \quad (3.1)$$

With the initial photon energy $E = 60 \text{ keV}$ and the rest mass of the electron $m_e c^2 = 511 \text{ keV}$ it follows:

$$E_{\text{CE},60 \text{ keV}} = 11.4 \text{ keV}.$$

The events with larger energies result from Doppler broadening due to the initial electron velocity.

The Compton distribution can be further distinguished into forward and backward scattered photons. The events in the left half of the Compton distribution are mostly forward scattered events ($\theta < 90^\circ$) and in the right half mostly backward scattered events ($\theta > 90^\circ$). This is because the X-rays lose more energy in the silicon detector for backward scattering than for forward scattering.

- **Multiple Compton scattering**

The amplitude of the distribution is much smaller than for single Compton scattering, because it is less probable to have multiple Compton scatterings in such a small volume. In first approximation, the distribution corresponds to the convolution of the single Compton distribution with itself.

- **Inverted Compton events**

The photon of an inverted Compton event passes the SDD, gets Compton scattered in the calorimeter, and is finally absorbed in the SDD. The scatter angle θ for these events is limited to $155^\circ \lesssim \theta \leq 180^\circ$. Events with a smaller angle would miss the SDD. Thus, their average energy loss in the calorimeter is a bit less than the maximum transferable energy for Compton scattering E_{CE} ($E_{\text{CE},60 \text{ keV}} = 11.4 \text{ keV}$). The energy distribution of the inverted Compton events in the SDD describes this behavior exactly. For 60 keV initial photons, the center of the distribution is at $\sim 50 \text{ keV}$.

- **Photoelectric absorption**

The large peak at 60 keV corresponds to photons, which are completely absorbed by the silicon detector. The small peak at $\sim 58 \text{ keV}$ is the silicon escape peak at which a fluorescence photon is emitted after the absorption. The difference in energy with respect to the main absorption line corresponds to the energy of the K_α line of silicon (1.74 keV). Events with total energies below the escape peak originate from electron escapes.

Table 3.1: Atomic lines of Br and Ce.

Line origin	Energy (keV)
Ce L $_{\alpha}$	4.8
Ce L $_{\beta}$	5.3
Br K $_{\alpha_{1,2}}$	11.9
Br K $_{\beta_{1,3}}$	13.3
Ce K $_{\alpha_2}$	34.3
Ce K $_{\alpha_1}$	34.7
Ce K $_{\beta_{1,3}}$	39.2
Ce K $_{\beta_2}$	40.2

- **Rayleigh scattering**

Rayleigh scattering is an elastic process where no energy is deposited. Thus, the main peak of the Rayleigh events is at 0 keV. Some energies of the Rayleigh events are in the same energy range like the Compton distribution. These are events with a Compton scattering before or after the Rayleigh scattering.

- **Secondary particles returning from the calorimeter**

The distribution of events with electrons returning from the calorimeter is flat compared to the one for photons. This is because the electrons interact continuously in the calorimeter before they leave its volume. For a photon escaping the CeBr₃ volume it is very unlikely that it has previously interacted. The initial energies of the secondary photons are determined by the atomic lines of the specific atom. Table 3.1 lists all atomic lines of cerium and bromine which can be clearly identified in the energy spectrum in figure 3.7.

Figure C.9 in the appendix shows the spectrum of the silicon detector from a simulation with a realistic Cygnus X-1 spectrum. The different components are analyzed as it is done for the monoenergetic beams. In view of the event selection in section 3.4.4, it should be noted that nearly all energies of inverted Compton events are less than 50 keV. These are the energies of photons after single Compton scattering in the calorimeter. The scatter angle θ has to be almost 180° that the photon hits the SDD. According to equation 3.1, 12 keV is the maximum energy deposit in the calorimeter for outgoing photons with 50 keV but the energy threshold of the calorimeter is at 10 keV. Therefore, most of the inverted Compton events cannot be measured.

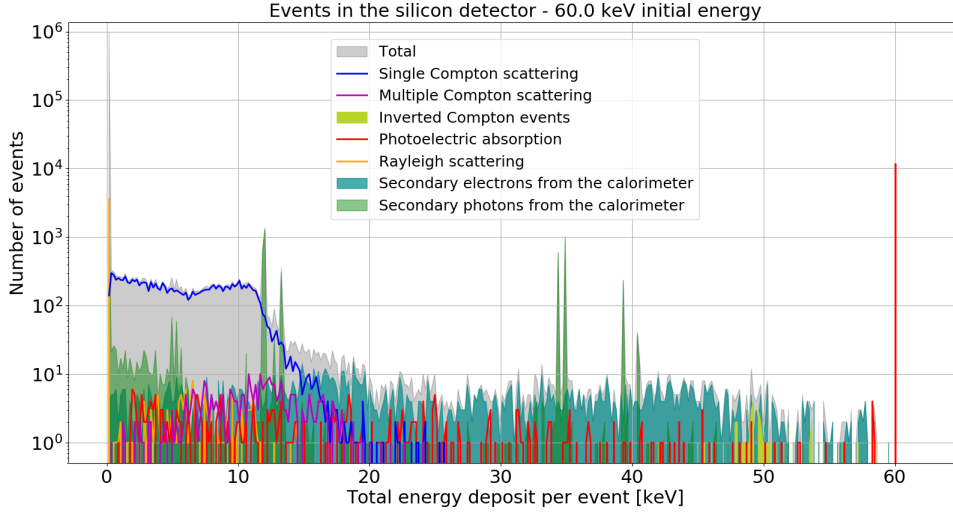


Figure 3.7: Simulated spectrum of the silicon detector for a 60 keV photon beam. The total spectrum is plotted as a gray area. Each event is assigned to a spectral component according to the two classification stages shown in figure 3.5 and 3.6. Each spectral component is plotted separately again. Resolutions and thresholds of the detectors are not taken into account.

3.4.2 Interaction types in the calorimeter

The classification for the calorimeter is analog to the one for the silicon detector. The X-ray of a Compton event is absorbed in the calorimeter after Compton scattering in the silicon detector. A visualization of the corresponding events is shown in the center part of figure 3.9. Events with multiple Compton scattering in the SDD are shown in the right part of figure 3.9. The left part of figure 3.9 shows events with Compton scattering in the calorimeter. These events potentially end up as inverted Compton events, with Compton scattering in the calorimeter and absorption in the silicon detector.

All event types of the calorimeter that cannot be used for polarimetry are shown in figure 3.6. The dominant process in the calorimeter is photoelectric absorption (left part of figure 3.6), e.g. absorption of the initial X-ray after passing the SDD without interaction. This class includes events with escaping secondary particles. The Rayleigh scattering events (center part of figure 3.6) are comparable to Rayleigh events in the silicon detector. Potential Compton events lose the polarization information due to the additional scattering. The last event class describes events with secondary particles coming from the silicon detector (right part of figure 3.6).

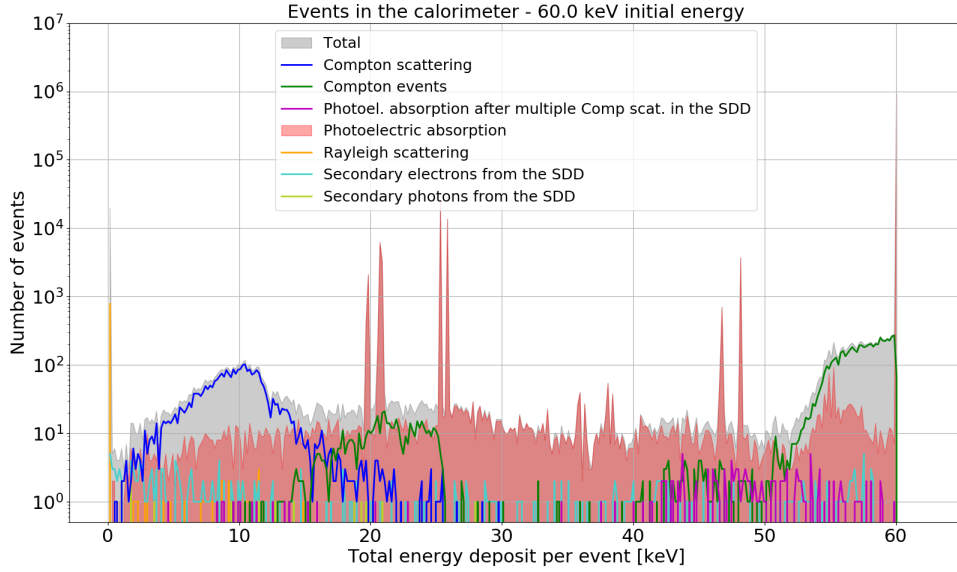


Figure 3.8: Simulated spectrum of the calorimeter for a 60 keV photon beam. The total spectrum is plotted as a gray area. Each event is assigned to a spectral component according to the two classification stages shown in figure 3.9 and 3.10. Each spectral component is plotted separately again. Resolutions and thresholds of the detectors are not taken into account.

Energy spectrum of the calorimeter

Figure 3.8 shows a spectrum of the CeBr_3 calorimeter. This spectrum is simulated with a monoenergetic 60 keV photon beam. It shows the total energy deposit per event for 10^6 simulated events. The complete spectrum as well as all mentioned event classes are displayed. Most of the following spectral features are energy dependent. The appendix C.1 contains spectra for different initial energies (30 keV, 100 keV, 150 keV, and 300 keV) for comparison.

- **Total energy spectrum**

The gray area in figure 3.8 has a peak at 0 keV. This is generated by events without interactions in the calorimeter, e.g. X-rays which are completely absorbed in the SDD. This peak rises for higher energies ($\gtrsim 90$ keV) because the absorption efficiency of the calorimeter decreases.

- **Compton scattering**

The Compton distribution in the calorimeter shows some differences to the one in the silicon detector. Equation 3.1 applies again for the description of the Compton edge. However, the low energy component (the forward scattered

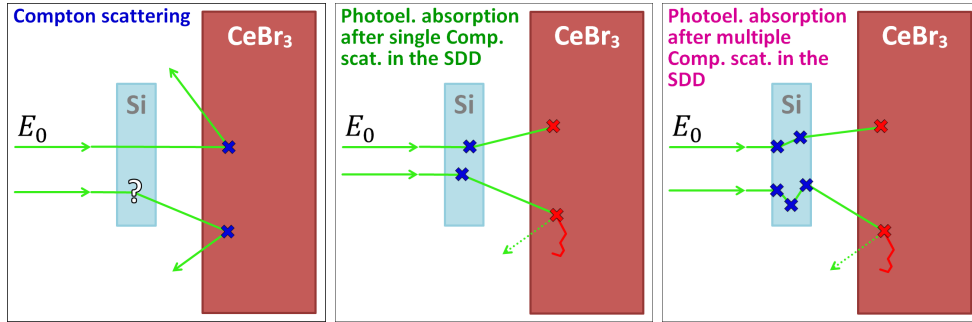


Figure 3.9: Visualization of events in the CeBr_3 calorimeter for the first stage of event classification. These events are potentially interesting for polarimetry. **Left:** The initial photon undergoes Compton scattering (blue cross) in the calorimeter and leaves it again. No other interactions take place in the calorimeter. The classification is regardless of interactions in the SDD. **Center:** The initial photon is absorbed (red cross) in the calorimeter after single Compton scattering in the SDD. These events are called **Compton events**. Events with a subsequent escape of secondary particles are included. **Right:** The initial photon is absorbed (red cross) in the calorimeter after multiple Compton scattering (blue cross) in the SDD. Events with a subsequent escape of secondary particles are included.

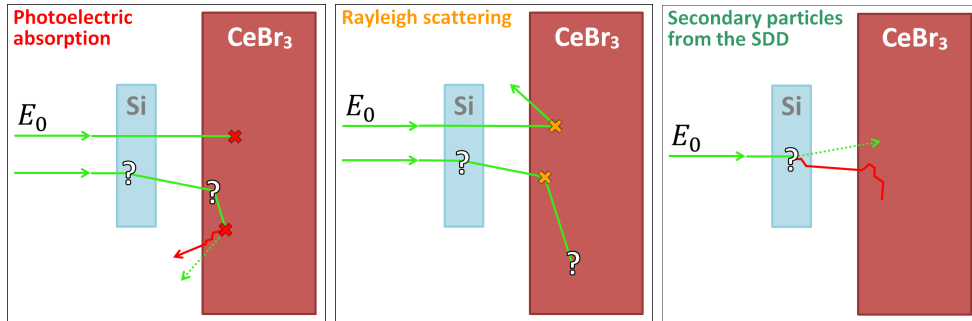


Figure 3.10: Visualization of events in the CeBr_3 calorimeter for the second stage of event classification. These events are not useful for polarimetry. **Left:** The initial photon is absorbed via photoelectric effect (red cross), regardless of interactions in the SDD. Events with further interactions before the absorption and events with escaping secondary particles are included. **Center:** The initial photon undergoes Rayleigh scattering (orange cross) in the calorimeter, regardless of interactions in the SDD and its further path. **Right:** The initial photon does not reach the CeBr_3 volume but secondary particles from the interaction in the silicon detector hit the calorimeter.

photons) of the Compton distribution is missing. That is because the stopping efficiency of the calorimeter is still very good at 60 keV. X-rays which undergo Compton scattering in the calorimeter with $\theta < 90^\circ$ are absorbed deeper inside the volume. Only photons which are backward scattered in a layer near to the detector surface can escape the volume again. Thus, the Compton distribution consists of backward scattered photons only. This behavior is energy dependent, as the calorimeter becomes transparent for higher $\gtrsim 90$ keV. From then on the forward scattered photons start to appear in the spectrum.

The events with a Compton scattering in the calorimeter are potential inverted Compton events, where the two detectors exchange their intended functions. This is the case when the X-ray gets backscattered and subsequently absorbed in the SDD.

- **Compton events**

This event class describes the best events for polarimetry. The X-rays undergo single Compton scattering in the SDD and are subsequently absorbed in the calorimeter. The distribution in the spectrum consists of two components. One component describes the completely absorbed photons. It is located between ~ 50 keV and 60 keV. The second component can be found at lower energies from ~ 15 keV to 25 keV and corresponds to events with emission of a fluorescence photon after the absorption. It is located directly below the two most dominant X-ray escape lines of cerium (K_{α_1} and K_{α_2}) at ~ 25 keV. In general, this happens at all escape peaks but not as pronounced as for the very dominant K_α lines of cerium.

- **Multiple Compton scattering in the SDD and absorption in the calorimeter**

Similar to the distribution in the SDD spectrum, the amplitude of the multiple Compton distribution is smaller and the width of the distribution is broader than the one for single Compton scattering.

- **Photoelectric absorption**

The large peak at 60 keV corresponds to photons passing the silicon detector without energy loss and subsequent complete absorption in the calorimeter. The continuous distribution over the complete energy range represents events with an electron escape from the calorimeter. Moreover, the discrete lines in the distribution are photon escape peaks. The lines can be identified with table 3.1. Since these are escape lines, the energy difference between the initial energy (60 keV) and the peak position has to be compared with the energy values of the atomic lines in the table.

- **Rayleigh scattering**

The Rayleigh distribution in the calorimeter spectrum shows the same behavior as in the SDD spectrum. As expected, the dominant peak is located at 0 keV and the spectrum shows an imitation of the Compton spectrum due to events with Compton and Rayleigh scattering (not as pronounced as for the SDD spectrum).

- **Secondary particles coming from the SDD**

The amount of events with secondary particles coming from the silicon detector is very small compared to the analog case in the SDD spectrum. This can be explained by the small detector volume of the SDD. The total amount of interactions in the silicon detector is smaller and therefore less secondary particles are produced compared to the amount of secondaries produced in the calorimeter.

Figure C.10 in the appendix shows the spectrum of the CeBr₃ detector from a simulation with a realistic Cygnus X-1 spectrum. The different components are analyzed as it is done for the monoenergetic beams.

3.4.3 Rate analysis

This section describes the rates of interesting processes in the detector. This is done on the basis of the event classification in the previous section.

Figure 3.11 shows the relative rate of processes over the energy of the incident photon. The detector response described in section 3.3 is not taken into account. The caption of the figure includes a detailed description of the rates. Only the most important ones are discussed here.

- **Compton events**

The rate of Compton events strongly decreases for energies below 20 keV. The reason for this is the decreasing cross section of incoherent scattering (Compton scattering at bound electrons), shown in left part of figure 1.4. The maximum of the rate is at ~ 90 keV. At this energy, about 0.6% of the incoming X-rays end up as Compton events. The slow rate reduction for larger energies can be explained by the decreasing absorption efficiency of the calorimeter.

- **Inverted Compton events**

The rate of inverted Compton events is smaller than 0.01% for all energies. It has its maximum at ~ 30 keV. As for the Compton events, the rate vanishes below 20 keV due to the low cross section of incoherent scattering. The rate also decreases towards large energies despite the strongly increasing rate for Compton scattering in the calorimeter. This is caused by the low absorption efficiency of the SDD for large energies.

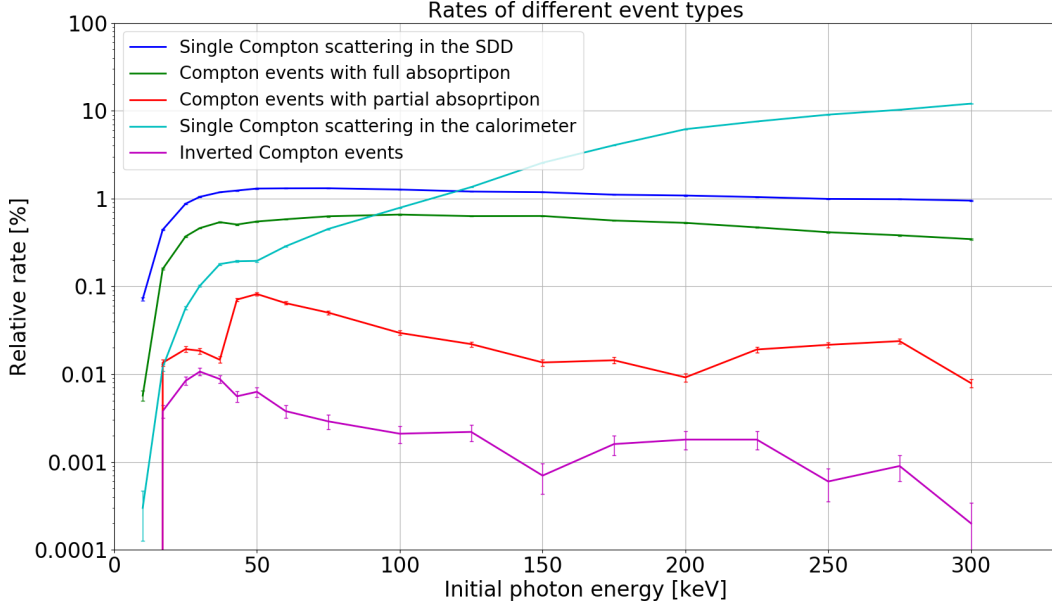


Figure 3.11: Relative rate of processes over the energy of the initial X-rays. About 1% of the incoming photons undergo single Compton scattering in the silicon detector (blue curve). Approximately half of these photons are subsequently completely absorbed in the calorimeter (green curve). The rate of these Compton events decreases for increasing energy because the absorption efficiency of the calorimeter decreases. The rate of Compton events with escaping secondary particles (red curve) increases stepwise at ~ 35 keV. This is because the intensive K_{α_1} and K_{α_2} line of cerium contributes for larger energies. The strongly increasing rate of single Compton scatterings in the calorimeter (turquoise curve) can be explained by the decreasing absorption efficiency of both detectors. For higher energies, more photons can pass the SDD and also more forward scattered photons can pass the calorimeter without being stopped. The rate of inverted Compton events (pink curve) is very low ($< 0.01\%$). It decreases at the energy of the Ce K_{α_1} and K_{α_2} line because events with photon escape are excluded for the analysis. Despite the increasing rate of Compton scatterings in the calorimeter, the rate of inverted Compton events decreases for higher energies. The reason is the strongly decreasing absorption efficiency of the SDD. The significant reduction of all rates for energies < 20 keV is due to the vanishing cross section of incoherent scattering for low energies (see figure 1.4).

In summary it can be said that the rate of Compton events reaches a useful level at energies $\gtrsim 20$ keV. After reaching its maximum of 0.7 % at 90 keV, the rate decreases towards larger energies. It is still on a significant level (0.4 %) at 300 keV. The relative rate of the inverted Compton events is a factor 100 lower than the rate of the normal Compton events. Thus, their contribution is not significant.

3.4.4 Event selection

As a first step, it is important to make a decision about which events to keep for the polarization analysis. In this work, only Compton events with complete absorption in the calorimeter are used for the analysis. The following list explains the underlying argumentation for all event types that can theoretically be used for polarimetry:

- **Compton events with complete absorption**

These events represent the simplest event type for polarimetry. For a single Compton scattering in the SDD and a complete absorption in the calorimeter no additional effects have to be considered. Furthermore, these events have the highest rate compared to alternative event types.

→ **Favored event type for the analysis.**

- **Compton events with partial absorption**

The possible missing energies for photon escapes are defined by the energies of the atomic lines of the material. The reconstruction of these events is similar to the Compton events with complete absorption. The energy measured by the calorimeter has to be increased by the energy of a dominant X-ray line. This procedure also increases the amount of wrongly selected events.

The overall rate of Compton events with any escape is less than 10 % of the rate with complete absorption (see figure 3.11). Therefore, the maximum possible contribution is on the scale of a few percent. The goal of this thesis is to estimate the order of magnitude of the sensitivity and not to supply the final analysis routine.

→ Not taken into account for the analysis.

- **Multiple interactions in the SDD**

The rate of clearly identifiable events with multiple interactions in the SDD is very low. This makes it unprofitable to consider these events for the polarization analysis.

→ Not taken into account for the analysis.

- **Inverted Compton events**

The reconstruction of these events is as simple as for the normal Compton events. However, it is not feasible to consider these events for polarimetry. The first reason is the very low rate (see figure 3.11). The second reason is the energy threshold of the calorimeter. The majority of the small Compton energies cannot be measured by the calorimeter (see last paragraph of section 3.4.1). The third and last reason is the decreasing polarization dependence for scatter angles $\theta \rightarrow 180^\circ$ (compare equation 1.2).

→ Not taken into account for the analysis.

As it is shown in section 3.4.3, less than 1% of the incident X-rays undergo single Compton scattering and subsequent full absorption in the calorimeter. Therefore it is important to have a precise selection of these Compton events. To obtain a good sensitivity on the polarization, a second cut, on the scatter angle itself has to be introduced. Figure 1.8 in section 1.2.2 shows the angular dependence of incoherent scattering. The modulation of the azimuthal distribution vanishes for small scatter angles θ . Therefore, the polarization signal is intensified by removing events with small scatter angles.

These two levels of the event selection are discussed in the following sections. It only affects the events with energy depositions in both detectors, which is about 0.8% of all events.

3.4.4.1 Selection of Compton events

For each event, the cosine of the scatter angle θ is reconstructed from the energy deposits E_{SDD} and E_{Cal} in the two detectors. The resulting angle is labeled θ_{E} . The details of the event reconstruction are explained in section 1.2.1. Additionally, it is possible to calculate θ from the two interaction positions R_{SDD} and R_{Cal} . For this method it is necessary to know the orientation of the satellite with respect to the source. This is given as ComPol will have a star tracker on board. The scatter angle resulting from the second method is labeled θ_{Pos} . The energy deposits and interaction positions of an actual Compton event, fulfill the following condition:

$$\Delta \cos \theta = \cos \theta_{\text{Pos}}(R_{\text{SDD}}, R_{\text{Cal}}) - \cos \theta_{\text{E}}(E_{\text{SDD}}, E_{\text{Cal}}) = 0 \quad (3.2)$$

All events which do not fulfill this condition inside a certain tolerance range are rejected. This method is applied to the cosine of the angles and not to the angles themselves because the energy resolution of the detectors can cause $\cos \theta_{\text{E}} > 1$ even for Compton events.

Figure 3.12 shows the distribution of $\Delta \cos \theta$. The peak of the Compton events around $\Delta \cos \theta = 0$ is very pronounced. Only a small percentage of other events is

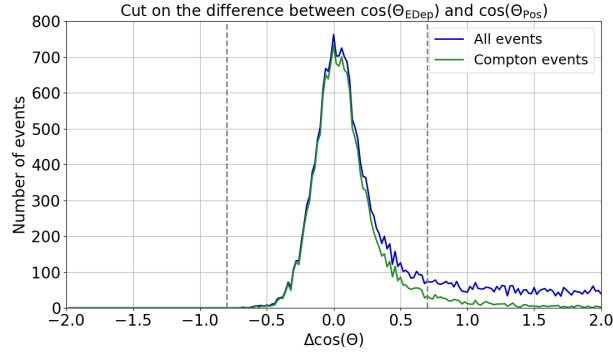


Figure 3.12: Selection of Compton events from the signal simulation data. The scatter angle θ is determined from the interaction positions and from the energy deposits in the two detectors. The difference $\Delta \cos \theta$ between these two angles is expected to be zero for a Compton event (see equation 3.2). The presented distribution is generated with a simulation of a realistic Cygnus X-1 source and the complete implementation of the detector response (described in section 3.3)

distributed around zero. Most of them lie outside the displayed area. The dashed lines show the applied tolerance range:

$$\Delta \cos \theta \in [-0.8, 0.7]. \quad (3.3)$$

The positive and negative threshold are set to the positions, where an enlargement of the range leads to more wrongly accepted events than correctly accepted Compton events. Since there is no background, the acceptance range can be chosen large. It has to be further restricted for the case with background radiation, as described in section 3.5.2.

To quantify the selection efficiency, the relative numbers of Compton/other events and rejected/accepted events are shown in Table 3.2. The total number of events in this table refers to the number of events with energy deposits in both detectors. It can be seen that 95% of the Compton events are accepted and 9% of all accepted events are wrongly accepted. The rates for the case with background radiation are discussed in section 3.5.2.1.

With additional background, the selection efficiency depends on the peak width of the $\Delta \cos \theta$ distribution. A narrower peak allows to reduce the width of the acceptance range. To compare the impacts of the energy resolution, position resolution, and energy thresholds, table 3.3 shows the **F**ull **W**idth at **H**alf **M**aximum (**FWHM**) of the respective $\Delta \cos \theta$ peak. The strongest broadening is due to the position resolution. This effect could be reduced by increasing the distance of the two detector

Table 3.2: Relative rates of acceptance/rejection of Compton/other events. The rates result from the analysis of the signal data. The total number of events refers to the number of events with energy deposits in both detectors.

	Compton events	Other events	
Accepted	30.5 %	3.0 %	33.5 %
Rejected	1.5 %	65.0 %	66.5 %
	32.0 %	68.0 %	100 %

Table 3.3: FWHM of the $\Delta \cos \theta$ peak as a measure of the impact of the different detector properties: energy resolution ΔE , position resolution ΔR , and energy thresholds E_{thres} .

Implemented settings	FWHM
Ideal case	0.06
ΔE	0.11
ΔR	0.33
E_{thres}	0.06
$\Delta E, \Delta R, E_{\text{thres}}$	0.39

layers, which would improve the angular resolution. The number of events would decrease simultaneously, because the second detector covers a smaller solid angle.

3.4.4.2 Selection of events with large scatter angles

The measurable scatter angles are defined by the geometry of the detector set-up. The minimum scatter angle is $\theta_{\text{min}} = 0^\circ$ for ComPol. The maximum possible scatter angle θ_{max} ranges from 72.6° to 85.5° , depending on the azimuthal direction and the interaction depth. The absolute maximum of 85.5° is only possible for a photon which Compton scatters in a corner of the SDD and is further on absorbed in the diagonally opposite corner of the calorimeter. This is only possible at the four corners. To get a more meaningful maximum angle it is necessary to average over the maximum angle in all azimuthal directions. For this, the interaction point is assumed to be in the center of the SDD. The maximum scatter angle also depends on the interaction depth in the calorimeter. The average interaction depth is energy

dependent. Low energetic photons are absorbed near the surface. Photons with higher energies penetrate further into the calorimeter. For the following, the analysis plane in the calorimeter is placed at the average interaction depth ($\bar{d}_{\text{int}} = 0.5 \text{ mm}$) determined from simulations. By averaging over the maximum scatter angles from the center of the SDD to the edge of this analysis plane in all azimuthal directions, θ_{max} results as:

$$\theta_{\text{max}} = 83.0^\circ. \quad (3.4)$$

The strongest modulation of the distribution of the azimuthal scatter angle Φ is received from events with large scatter angles ($\theta \approx 90^\circ$). The azimuthal modulation vanishes for scatter angles $\theta \rightarrow 0^\circ$ (compare figure 1.8). Therefore it is advisable to exclude events with low scatter angles from the polarization analysis. To obtain the best possible sensitivity, it is important to balance between the number of events and the grade of modulation. Muleri & Campana [42] showed analytically the best selection criteria (equation 3.5).

$$\theta > \theta_{\text{min}}^{\text{opt}} = 0.57 \cdot \theta_{\text{max}} \quad (3.5)$$

With equation 3.4 results $\theta_{\text{min}}^{\text{opt}} = 47.3^\circ$ as the best lower limit for the scatter angle. It is possible to verify this optimum with the simulated data. Therefore, the polarization analysis (section 3.4.5) and the sensitivity calculation (section 3.6) are performed for different selection criteria. The results from a scan over the parameter space (from 0° to 90°) of $\theta_{\text{min}}^{\text{opt}}$ show the best polarization sensitivity for

$$\theta > \theta_{\text{min}}^{\text{opt}} = 55^\circ. \quad (3.6)$$

With the relation in equation 3.5, it leads to an impossible maximum scatter angle $\theta_{\text{max}} = 96^\circ$. This discrepancy is explained by the 1 keV energy threshold of the silicon detector. A 30 keV photon, Compton scattered at an angle of 47° deposits only 0.55 keV in the SDD. Moreover, the simulated spectrum of Cygnus X-1 increases towards low energies. Therefore, many Compton events can not be measured even for scatter angles wider than the analytical optimum of 47.3° . The resulting effect is a larger optimum cut value determined from the data.

The minimum angle determined from the simulation data is used for the further analysis. The distribution of the scatter angles θ of the signal events which passed the first selection stage (see section 3.4.4.1) is shown in figure 3.13. The dashed line shows the lower limit $\theta_{\text{min}}^{\text{opt}}$ for the event acceptance.

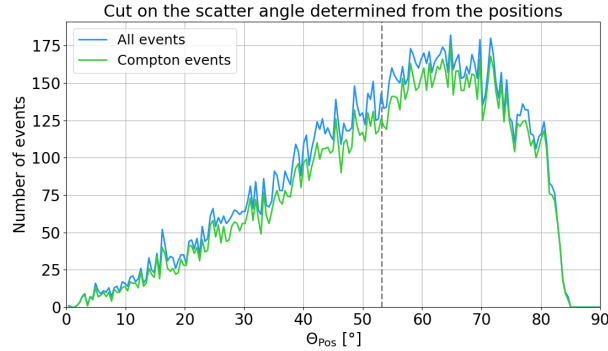


Figure 3.13: Selection of Compton events with large scatter angles. The minimum scatter angle for accepted events is indicated by the dashed line. The selection criteria (equation 3.6) for the scatter angle is applied to all events which passed the first selection stage (section 3.4.4.1). This is done because Compton events with large scatter angles θ show a stronger polarization dependence.

3.4.5 Polarization analysis

The polarization analysis is applied to all events which pass the event selection described in section 3.4.4. Figure 3.14 shows the distribution of the azimuthal scatter angle Φ of these events. The cosine modulation originates from the polarization dependent cross section of Compton scattering, as it is described in section 1.2.2. The Φ distribution is described by equation 1.8. The best function parameters are obtained from a fit. The impact on the modulation curve of the energy resolution, position resolution, and energy thresholds are shown in figure 3.15. The shown curves are normalized to the expected number of events for a one year observation of Cygnus X-1. Details on the normalization can be found in the appendix B.

The signal simulation yields the following final results for the modulation amplitude a and the signal rate R_S :

$$a = 0.62 \quad \text{and} \quad R_S = 3.4 \times 10^{-4} \text{ cps.} \quad (3.7)$$

In comparison, 0.46 cps is the total rate of photons coming from Cygnus X-1. Therefore, less than 1% of all incoming X-rays from Cygnus X-1 end up as Compton events and can be used for the polarization analysis.

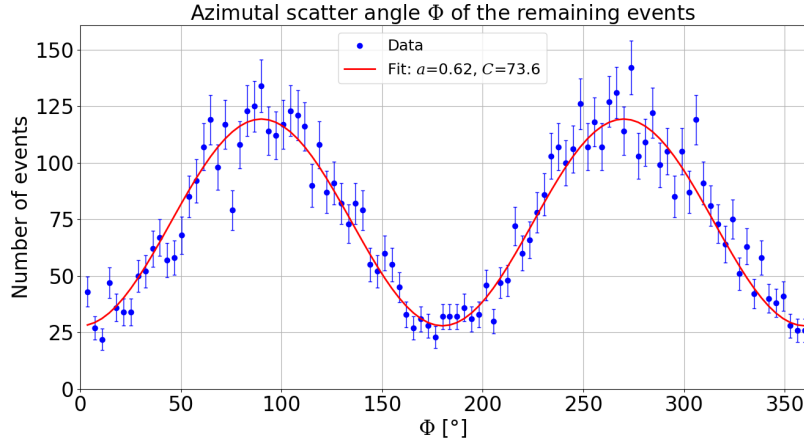


Figure 3.14: Distribution of the azimuthal scatter angle Φ for data from a simulation with a realistic Cygnus X-1 spectrum and with the realistic response of the two detectors. The distribution is described by the function in equation 1.8. The cosine modulation is the imprint of the initial X-ray polarization. The data is not yet normalized. The result normalized to 1 year is displayed in figure 3.15.

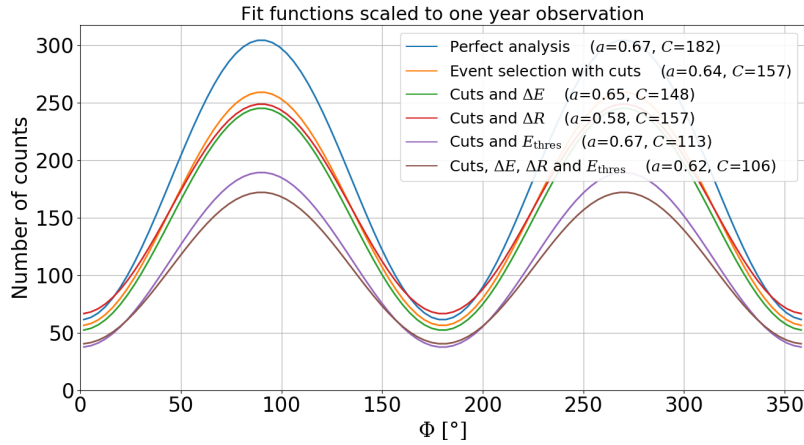


Figure 3.15: Description of Φ distribution according to equation 1.8. The curves are normalized to one year of observation time. The *perfect analysis* (blue curve) shows the polarization signal with the knowledge of the Monte Carlo truth. The orange curve illustrates the impact of the event selection (see section 3.4.4). The green, red, and purple line demonstrate the impact of different properties of the detector response (energy resolution ΔE , position resolution ΔR , and energy thresholds E_{thres}). The brown curve shows the most realistic case (realistic event selection and complete detector response). The function parameters in the legend are the respective values for the modulation amplitude a and the baseline C of the cosine (see equation 1.8).

3.5 Background simulation

Satellites are exposed to enormous background radiation. The particle energies reach beyond the TeV range. The impact of the background radiation is investigated in the following sections. Section 3.5.1 describes the real background sources and their implementation for the simulation. The subsequent section 3.5.2 is devoted to the event selection and section 3.5.4 concludes with a discussion about the remaining events and their rates.

3.5.1 Background sources

The particle spectra used for the background study are from measurements in a low Earth orbit (550 km) [41]. The simulation includes photons and the most abundant types of cosmic rays (electrons, positrons, protons, and alpha particles). The used spectra are displayed in figure 3.3 in section 3.2. For cosmic rays, it is possible to distinguish between a spectral component above and below ~ 5 GeV. The high energy component is mainly composed of primary cosmic rays. Most of them originate from supernovas outside our galaxy. The charged particles are accelerated by the shock waves of massive stellar explosions. The spectral component below ~ 5 GeV is dominated by secondary particles from the Earth's atmosphere.

The particle source in the simulation is a spherical surface around the detector set-up. The emission from the surface is according to the cosine emission law. This emission law is a possible option in Geant4. The necessary normalization for this kind of simulation is described in the appendix B.

3.5.2 Background exclusion

Only Compton events are used for the polarization analysis, as justified in section 3.4.4. Compton events are events with one single Compton scattering in the silicon detector and subsequent complete absorption in the calorimeter. Therefore only background events with energy deposits in both detectors are considered in the following event selection. This work investigates the sensitivity in the energy range from 10 keV to 300 keV. Thus, the energy deposits of a background event have to fulfill the condition:

$$E_{\text{SDD}} + E_{\text{Cal}} < 300 \text{ keV}. \quad (3.8)$$

Furthermore, the remaining background events have to fulfill the same criteria as the signal events to be accepted for the polarization analysis. The first selection stage selects the Compton events (section 3.5.2.1). The second stage (discussed in section 3.5.2.2) is for the selection of events with large scatter angles.

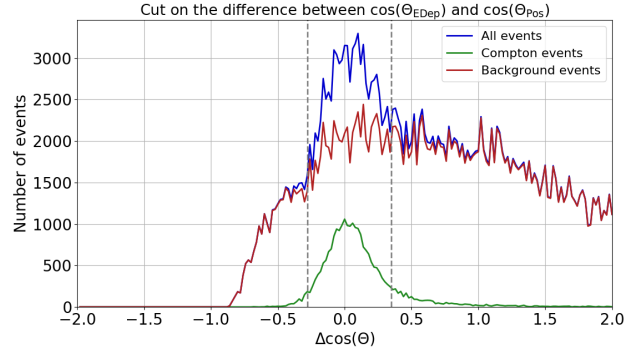


Figure 3.16: Selection of Compton events from the combined signal and background simulation data. Both data sets are normalized to 1 year observation time. The analog case without additional background radiation is shown in figure 3.12. The scatter angle θ is determined from the interaction positions and from the energy deposits in the two detectors. The difference $\Delta \cos \theta$ between these two angles is expected to be zero for a Compton event (see equation 3.2). The effects of the detector response are included as described in section 3.3.

3.5.2.1 First exclusion stage

The procedure of the first event selection stage is described in detail in section 3.4.4.1. The cosine of the scatter angle θ is determined from the energy deposits and from the interaction positions. The respective angles are labeled θ_E and θ_{Pos} . These two reconstruction methods lead to the same values for Compton events. Most of the background events fulfill the respective condition (equation 3.2) by chance. Only background photons which enter the detector system through the collimator can fulfill the condition as actual Compton events.

Figure 3.16 shows the distribution of the difference $\Delta \cos \theta$ between the two reconstructed angles. The datasets from the signal simulation and from the background simulation are combined for this plot. The background is present as a flat distribution compared to the peak of Compton events around $\Delta \cos \theta = 0$.

The acceptance range has to be restricted compared to the case without background radiation (see section 3.4.4.1). The best range (equation 3.9) was found by scanning the parameter space of the boundaries (from $\Delta \cos \theta = -1$ to $\Delta \cos \theta = 1$) and selecting the combination with the best final sensitivity on the polarization. The calculations for the sensitivity are described in section 3.6.

$$\Delta \cos \theta \in [-0.28, 0.35] \quad (3.9)$$

Table 3.4: Relative rates of acceptance/rejection of Compton/background events. The rates result from the analysis of the combined signal and background data. The total number of events refers to the number of events with energy deposits in both detectors.

	Compton events	Background events	
Accepted	3.0 %	9.5 %	12.5 %
Rejected	0.6 %	86.9 %	87.5 %
	3.6 %	96.4 %	100 %

To quantify the selection efficiency, the relative numbers of Compton/background events and rejected/accepted events are shown in Table 3.4. The total number of events in this table refers to the number of events with energy deposits in both detectors. It can be seen that 84 % of the Compton events are accepted and 76 % of all accepted events are wrongly accepted. The rate of accepted Compton events decreased by a few percent in comparison to the case without additional background radiation whereas the rate of wrongly accepted events increased by 67 %. For comparison, the rates for the case without background radiation are shown in table 3.2.

3.5.2.2 Second exclusion stage

Events with large scatter angles are selected in the second stage of the event selection. This is because the polarization dependence vanishes for small scatter angles θ . A detailed discussion of the selection criteria is done in section 3.4.4.2. The best cut value is found by scanning the parameter space from 0° to 90° and minimizing the final sensitivity. The resulting criteria is:

$$\theta > \theta_{\min}^{\text{opt}} = 55^\circ. \quad (3.10)$$

The determined value is in agreement with the one for the case without additional background.

The distribution of the scatter angles θ of the events which passed the first selection stage (see section 3.4.4.1) is displayed in figure 3.17. The dashed line shows the lower limit $\theta_{\min}^{\text{opt}}$ for the event acceptance in the second selection process.

The strong fluctuation of the background distribution compared to the distribution of the Compton events is due to the different simulated time scales. The signal simulation with 1×10^7 events corresponds to ~ 250 days of Cygnus X-1 observation. In contrast, the 1×10^{11} simulated background events correspond to a time scale of ~ 26 days. This was done to keep the simulation time and the output file size of the background simulation in a reasonable order of magnitude. It is still enough to obtain the order of magnitude of the background.

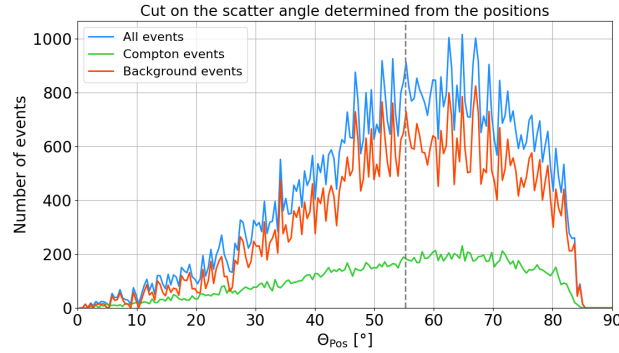


Figure 3.17: Selection of Compton events with large scatter angles from the combined data of signal and background simulation. Both data sets are normalized to 1 year observation time. The minimum scatter angle for accepted events is indicated by the dashed line. The selection criteria (equation 3.10) for the scatter angle is applied to all events which passed the first selection stage (section 3.5.2.1). This is done because Compton events with large scatter angles θ show a stronger polarization dependence.

3.5.3 Remaining background events

Figure 3.18 shows the initial energies of the background particles that deposited energy in the detector system. The dominant contribution comes from low energetic photons as expected from the simulated spectra (see figure 3.3). The rate of the electrons increases at 2 MeV. From there on, they have enough energy to pass through the solar panels. The same effect for protons is observable at 20 MeV. The higher threshold is explained by the larger mass of the proton. Furthermore, the positron spectrum does not show this characteristic because another effect comes into play. A positron, that is stopped in one of the solar panels, annihilates with an electron of the material. Two 511 keV photons are created from this annihilation. The produced photons have enough energy to reach the detector system.

Table 3.5 quantifies the contribution per initial particle type. The second column lists the total percentages of events with interaction in the detector system. The third column contains the fractions for events with energy deposits in the important energy range (10 keV to 300 keV). In this range, the photon contribution is even more dominant. Finally, the last column lists the percentages of events that passed the event selection. Here it is mentionable that positrons have a significant contribution ($\sim 18\%$) to the final background.

The energy spectra measured by the SDD and the calorimeter are displayed in the appendix C.3. The contribution of each initial particle type is plotted separately. A

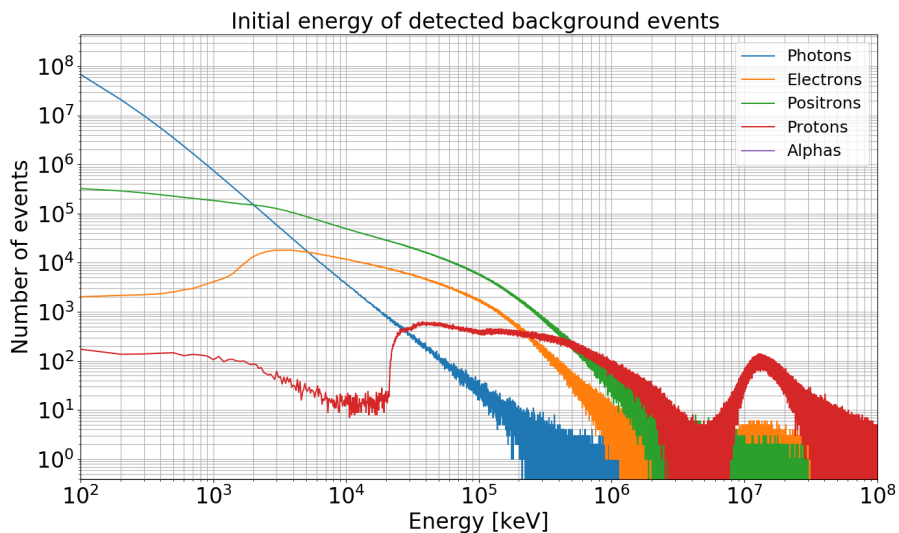


Figure 3.18: Initial energies of all background events with an energy deposit in the detector system. Each particle type is individually displayed.

Table 3.5: Composition of the measured background events. Analyzed for all background events, for those in the energy range of the signal (10 keV to 300 keV) and for those which are not excluded by the event selection.

Particle type	All events (%)	In the signal energy range (%)	Passing event selection (%)
Photons	84.4	96.8	71.2
Electrons	2.0	0.5	4.6
Positrons	8.8	2.3	18.3
Protons	4.3	0.3	3.7
Alphas	0.6	0.1	2.1

significant feature in the calorimeter spectrum is the 511 keV line of the photons from the electron positron annihilation. The two significant peaks in the SDD spectrum at 35 keV and 40 keV are caused by the K_α and K_β line of cerium. The broad peaks at ~ 150 keV in the SDD spectrum and ~ 7 MeV in the calorimeter spectrum are geometrical effects. They originate from the thickness of the respective detector. Charged particles with higher energies pass the detector and deposit a characteristic fraction of their initial energy in the detector.

Figure 3.19 visualizes the directions of the background particles that passed the event selection. The left part of the figure shows the projection of the origins on a plane perpendicular to the symmetry axis of the CubeSat and the right part shows the projection parallel to the symmetry axis. It becomes clear that particles from the backside are efficiently shielded by the material distribution behind the detector system. This distribution in the actual satellite will be less dense because the materials are spread over the two other CubeSat units. Therefore, the difference between particles from the front and from the backside will be less pronounced. Furthermore, the particle origins show an accumulation in front of the collimator. Background photons which enter through the collimator and end up as a Compton event cannot be shielded and therefore not distinguished from signal events.

3.5.4 Rate analysis

So far, only events with energy deposits in both detectors are considered. The simulation results may have to be corrected for random coincidence of two incoming events. Whether this is required depends on the rates measured by the two detectors:

$$f_{\text{SDD}} = 0.36 \text{ cps} \quad \text{and} \quad f_{\text{Cal}} = 134.0 \text{ cps.}$$

With equation 3.11 [43], it is possible to estimate the rate of randomly coinciding events.

$$f_{\text{RC}} = 2\tau f_{\text{SDD}} f_{\text{Cal}} \tag{3.11}$$

The coincidence time window is labeled with τ . The minimum window size is limited by the time resolution of the SDD. A plausible value is $\tau = 100$ ns. The rate for random coincidence results as $f_{\text{RC}} = 1 \times 10^{-5}$ cps. This is less than 1‰ of the rate of normal events with energy deposits in both detectors. Therefore, the effect of randomly coinciding events is negligible.

All background events that passed the event selection (described in section 3.5.2) are used for the further analysis. The signal data shows a cosine modulation in the distribution of the azimuthal scatter angle Φ . The background is not expected to be modulated. A slow rotation of the CubeSat around its longitudinal axis would even wash out possible systematics. For ComPol it is not finally decided if it will be operated in a spinning mode.

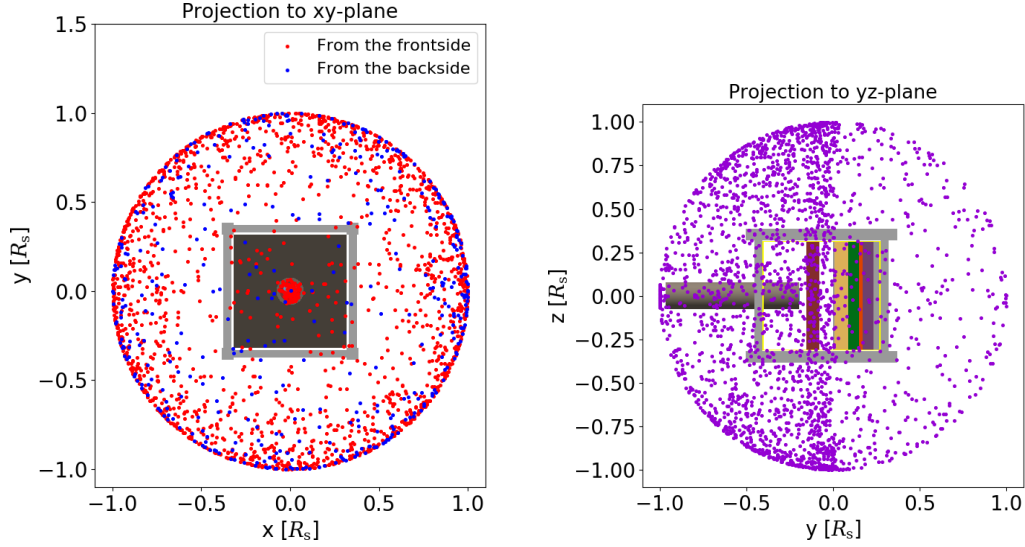


Figure 3.19: In the background simulation, the particles originate from a spherical surface around the CubeSat. The particle origins of the remaining background events are visualized as points on this surface. The coordinates are given in units of the spherical radius R_s .

Left: Projection of the particle origins on the xy -plane, transverse to the satellites symmetry axis. The red/blue dots show the particles originating on the front/back half sphere. It shows that a significant number of background particles enters the system through the collimator.

Right: Projection of the particle origins on the yz -plane, parallel to the satellites symmetry axis. The dummy material distribution of the CubeSat represents a significant shielding for particles coming from the backside.

The distribution of the Φ values for the data from the background simulation is displayed in figure 3.20. The distribution is fitted with a flat function. The height of the line is used for the further sensitivity study.

The background simulation yields the following final result for the rate R_B of background events that pass the event selection:

$$R_B = 1.0 \times 10^{-3} \text{ cps.} \quad (3.12)$$

In comparison, the signal rate is $R_S = 3.4 \times 10^{-4}$ cps. The resulting signal to noise ratio is:

$$\text{SNR} = 0.34 \quad (3.13)$$

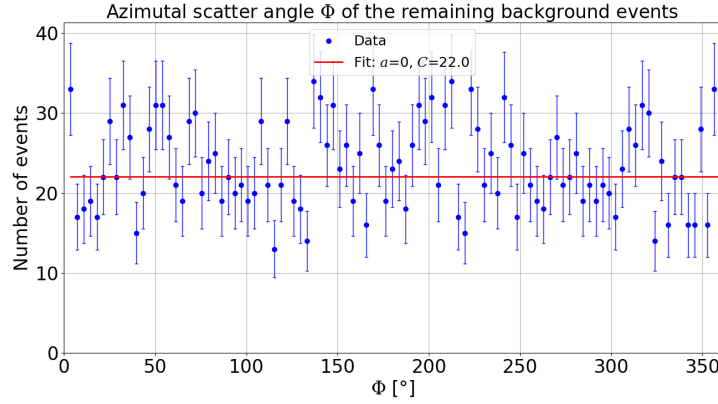


Figure 3.20: Distribution of the azimuthal scatter angles Φ for all background events that passed the event selection (section 3.5.2). No polarization and therefore no cosine modulation is expected for the background events. Thus, the data is described with a flat function. The distribution is not yet normalized. The rate after normalization is stated in equation 3.12.

3.6 ComPol's polarization sensitivity

This section describes the analysis concerning ComPol's sensitivity on the polarization of Cygnus X-1 in the energy range from 10 keV to 300 keV. The sensitivity is determined on two different ways. The first way is with the χ^2 -method and the second way uses the **Minimum Detectable Polarization (MDP)**. The two methods are described and compared in section 3.6.1. Section 3.6.2 is devoted to the effects of the detector response on the sensitivity. The results for different energy ranges are presented in section 3.6.3 and section 3.6.4 concludes with the impact of the background.

3.6.1 Determination of the sensitivity

The sensitivity is determined with two different methods:

1. χ^2 -method:

Equation 1.8, describes the distribution of the azimuthal scatter angle Φ . The best fit parameters are obtained in section 3.4.5. The cosine modulation of this distribution is the imprint of the polarization signal. Since the signal simulations are done with 100% polarized light, the obtained curves display the maximum possible modulation with modulation amplitude μ .

By scaling the modulation amplitude μ with the factor P ($0\% \leq P \leq 100\%$),

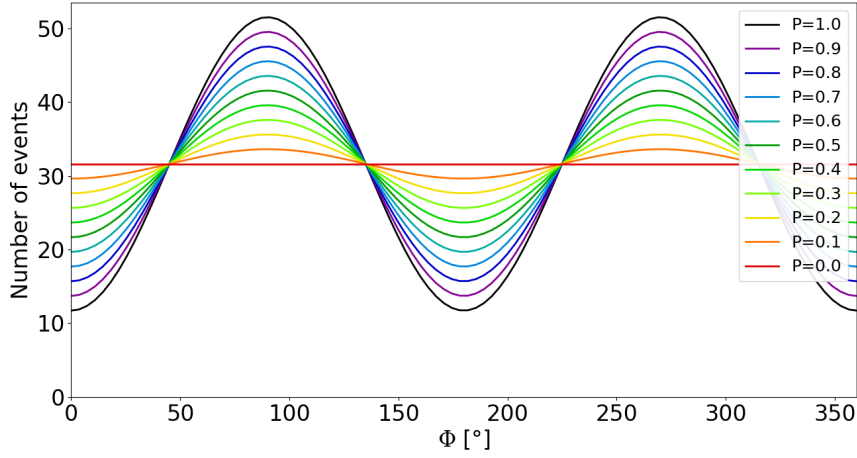


Figure 3.21: The fit function obtained from the signal simulation with 100 % polarized light is scaled to lower degrees of polarization P .

it is possible to generate the expected data for different degrees of polarization. The value of P directly corresponds to the degree of polarization. For small degrees of polarization it is just an approximation. The reason is that the best fitting modulation amplitude for a flat distribution with statistical fluctuations is always larger than zero. This effect is neglected for the further analysis. The scaling for different degrees of polarization is visualized in figure 3.21.

The next step is to calculate the χ^2 between the flat function (unpolarized distribution) and a curve with $P > 0\%$. Equation 3.14 defines χ^2 as:

$$\chi^2 = \sum_i^{N_{\text{bins}}} \left(\frac{f_{0,i} - f_{P,i}}{\sigma_i} \right)^2. \quad (3.14)$$

The number of bins is denoted with N_{bins} and σ_i is the uncertainty for each bin. The measured values per bin are assumed to be Poisson distributed. Therefore, it results:

$$\sigma_i = \sqrt{f_{P,i}}. \quad (3.15)$$

The polarization value $P_{3\sigma}$ of the curve for which $\chi^2 = 9$ corresponds to the 3σ sensitivity polarization limit.

The dependence on the observation time can be investigated by scaling the factor C in the functions f_0 and f_P . The C value depends on the number of simulated events and has to be normalized as it is described in the appendix B.

The impact of the background on the total Φ distribution is equal to a flat contribution. Therefore, the polarization curve obtained from the signal simu-

lation is shifted by the normalized C value of the background data. This shift leads to a smaller χ^2 value because the uncertainties σ_i increase.

2. Minimum detectable polarization:

The **Minimum Detectable Polarization (MDP)** is a common parameter in X-ray polarimetry. It describes the 3σ sensitivity in the absence of instrumental systematic effects [44]. Equation 3.16 defines the MDP depending on the observation time T .

$$\text{MDP} = \frac{4.29}{\mu \cdot R_S} \left(\frac{R_S + R_B}{T} \right)^{1/2} \quad (3.16)$$

The rates of signal and background events are labeled R_S and R_B . The maximum possible modulation amplitude for a 100 % polarized beam without background is denoted with μ .

All results from the signal and the background analysis, which are necessary to determine the sensitivity are summarized in table 3.6. Since the simulation was done with a 100 % polarized beam, the determined modulation amplitude a corresponds to the maximum possible signal modulation μ .

Table 3.6: Summary of all values necessary for the final sensitivity calculation.

Parameter	Value
Modulation amplitude a	0.62
Signal rate R_S	3.4×10^{-4} cps
Background rate R_B	1.0×10^{-3} cps

In figure 3.22, the 3σ sensitivity limit determined with the χ^2 -method is compared to the MDP. The plot shows the evolution of both over time. The two methods show a very good conformity. The two values for the sensitivity limit after one year are:

$$P_{3\sigma}^{\chi^2} = 13.2\% \quad \text{and} \quad P_{3\sigma}^{\text{MDP}} = 13.3\%.$$

This means, it is necessary to take at least one year of data, to be sensitive to a degree of polarization of 13 %. The investigations in the following sections are done with the χ^2 -method.

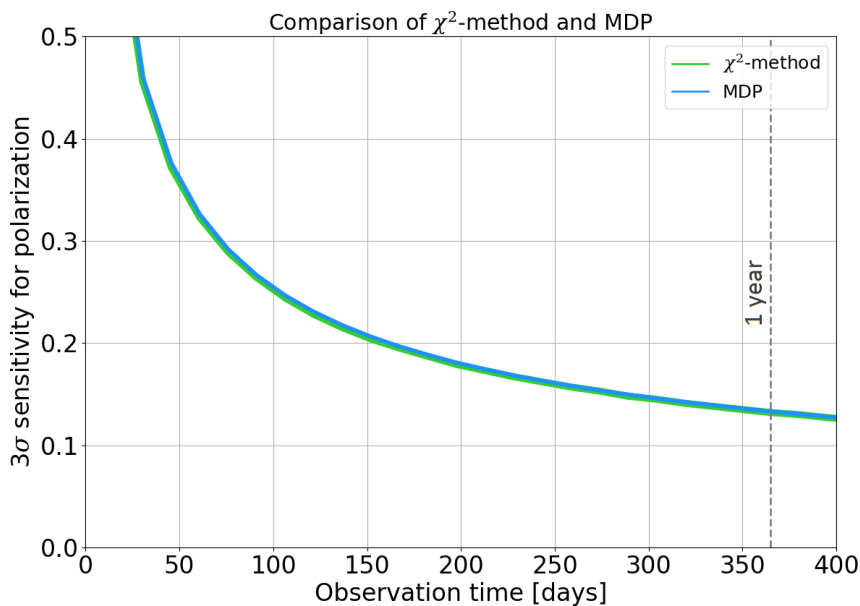


Figure 3.22: Comparison between the χ^2 -method and the Minimum Detectable Polarization (MDP). Each line describes the 3σ sensitivity on the polarization over the observation time of Cygnus X-1. The two functions match perfectly.

3.6.2 Effects of the detector response on the sensitivity

In this section, the effects of the detector properties are investigated. Figure 3.23 shows the sensitivity for different implementations of the detector response. The detectable degree of polarization is plotted over the observation time. The analysis does not include effects of the background radiation.

The result demonstrates that the energy resolution has nearly no impact on the final sensitivity. It is only slightly above the case with an ideal detector response. The strongest influence has the position resolution. Its impact is approximately six times larger than the impact of the energy resolution. The position resolution causes a washout of the modulation in the Φ distribution. This effect can be reduced by placing the detectors further apart, which increases the angular resolution.

3.6.3 Energy dependence of the sensitivity

ComPol will observe Cygnus X-1. The sensitivity on its polarization strongly depends on the considered energy range. This energy dependence is introduced by the energy thresholds of the detectors, by the relative rate of Compton events (described in section 3.4.3), and by the spectrum of Cygnus X-1 (see figure 3.2). The thresholds

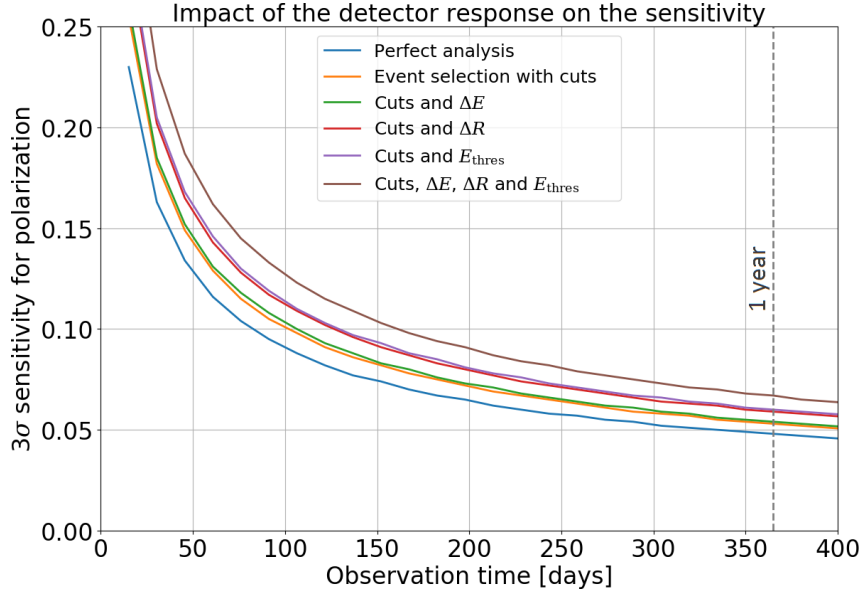


Figure 3.23: The 3σ sensitivity is plotted over the observation time in days. It is shown for different implementations of the detector response. No background effects are included. The *perfect analysis* shows the situation with knowledge of the Monte Carlo truth. All other lines are generated by applying the event selection described in section 3.4.4. These lines show the result of the event selection itself, of the energy resolution ΔE , the position resolution ΔR , and of the energy thresholds E_{thres} . The brown line, shows the sensitivity limit for the complete detector response. The energy resolution has nearly no impact on the final sensitivity. The position resolution has the strongest impact compared to the other investigated properties.

and the rate of Compton events limit the operation range of ComPol towards low energies at ~ 25 keV. On the other side, the operation range of ComPol is limited by the quickly decreasing flux of Cygnus X-1 towards higher energies. The relative effect of the considered energy range is presented in figure 3.24. The results are generated from simulations with monoenergetic photon beams. The resulting polarization curves are weighted according to the spectrum of Cygnus X-1 for a one year observation. The weighting corresponds to the flux of Cygnus X-1 in a 10 keV large energy range centered around each simulated energy. The resulting polarization limits display the relative contributions to the total polarization sensitivity. The strongest contribution comes from the energies around 40 keV.

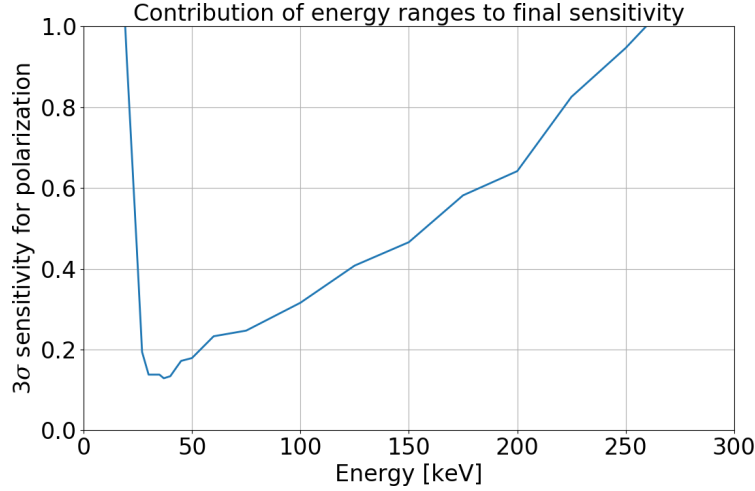


Figure 3.24: The 3σ sensitivity for a one year observation is plotted over the energy. Background effects are not included. The results are obtained from simulations with monoenergetic photon beams, which are weighted by the spectrum of Cygnus X-1. The weighting factors corresponds to the flux of Cygnus X-1 in a 10 keV large energy window centered around each simulated energy. The resulting polarization limits display the relative contributions to the total polarization sensitivity.

3.6.4 Impact of the background on the sensitivity

This section describes the impact of the background. The background level is included in the analysis as explained in section 3.6.1. Figure 3.25 shows the sensitivity for different background rates. The signal to noise ratio determined in this thesis worsens the sensitivity by 7% degree of polarization. It ends up at 13% after one year of observation time.

For Cygnus X-1, a weak polarization ($\lesssim 25\%$) is expected in the investigated energy range. Therefore, it would be beneficial to further increase the signal to noise ratio from 0.34 to ~ 1 . This would improve the sensitivity after 1 year by almost 4%. In summary it can be said, that the background is crucial for the final polarization sensitivity of ComPol.

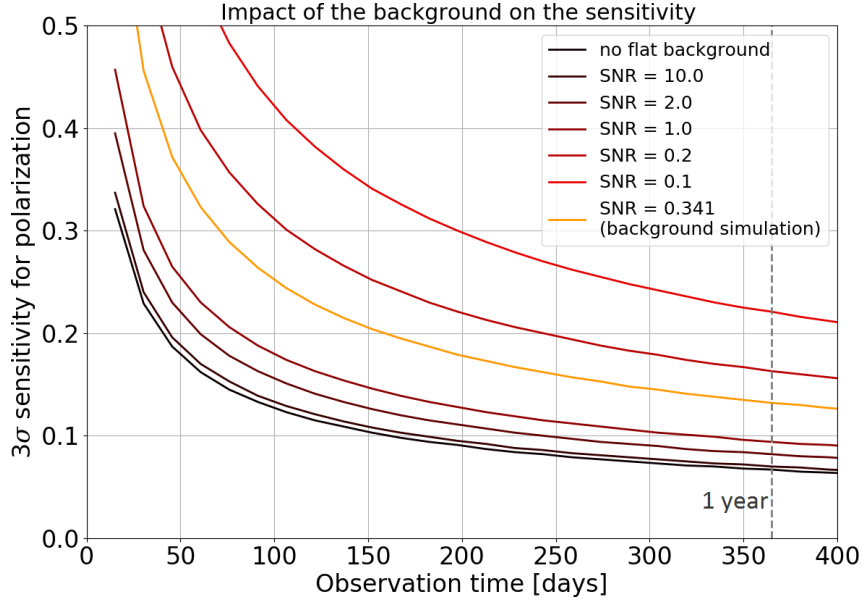


Figure 3.25: The plot shows the 3σ sensitivity limit over time for different background rates. The black line displays the polarization limit for the situation without background, the orange line for the background rate determined from the background simulation. The other lines show the situation for different artificial **S**ignal to **N**oise **R**atios (**SNR**).

3.7 Conclusions

The results of the sensitivity study show the feasibility of the ComPol project. The sensitivity on the polarization after 1 year of observation is at the order of magnitude which is expected for Cygnus X-1 ($P \lesssim 25\%$). The sensitivity should be improved to further increase the chance of success for the project. The results do not demonstrate the final sensitivity of the instrument. They provide a first estimation of the expected signal and background rate and thereby an excellent basis for further design optimizations. The outcome confirm the chosen detector system to be suitable for the specific application in ComPol. The instrument can collect data on the polarization down to ~ 25 keV. The study demonstrates that a large **S**ignal to **N**oise **R**atio (**SNR**) is the most crucial factor for the final sensitivity. The analysis of the background simulation yields a SNR of 0.34. This ratio can be further improved by refining the detector geometry. Reaching a SNR of 1 would be beneficial for the success chance of the ComPol project.

Chapter 4

Summary and outlook

The ComPol project is a CubeSat mission which aims at measuring the polarization of the hard X-rays from the black hole binary system Cygnus X-1. Detailed design studies are required to optimize the instrument's performance despite the strong size and weight limitations for CubeSat experiments. This work investigates the reachability of the scientific goal. The results are based on Monte Carlo simulations performed with Geant4.

The study performed for this thesis contains a detailed event classification. These event classes are extensively discussed in terms of their usefulness for polarimetry. The applied event reconstruction and event selection is described in detail and compared for the situation with and without radiation background. Finally, ComPol's sensitivity on the polarization of Cygnus X-1 is determined with two different methods, with a χ^2 -test and with the **Minimum Detectable Polarization (MDP)**. The MDP is a common parameter for the statistical analysis in polarimetry. The two results are matching perfectly. Furthermore, the dependence on the considered energy range is discussed and the impact of the detector response and the radiation background are studied.

The outcome of the sensitivity study shows the feasibility of the ComPol project. It is possible to compensate the small detector area ($A_{\text{SDD}} \approx 1 \text{ cm}^2$) of the CubeSat experiment with a long observation time (~ 1 year). The resulting minimum detectable polarization at a 3σ level is at 13% for a one year observation. Cygnus X-1 is expected to have weak polarization ($\lesssim 25\%$) in the hard X-ray range. For the sensitivity result, the spectrum of Cygnus X-1, the detector response, and the expected background radiation in a low Earth orbit are simulated. The background simulation yields a **Signal to Noise Ratio (SNR)** of 0.34. The analysis demonstrates that a high SNR is crucial for the final sensitivity.

Several options should be considered to optimize the SNR and improve ComPol's polarimetric performance. A possible way would be to include more event types in the analysis. In this thesis, only Compton events were used: single Compton scattering in the silicon detector and subsequent complete absorption in the calorimeter. The total signal rate can be increased by including more event types in the analysis,

e.g. events with an escaping fluorescence photon from the calorimeter. It has to be investigated whether an inclusion of these events leads to a better signal to noise ratio.

Increasing the rate of Compton events could be also possible by geometrical modifications, e.g. stacking a second SDD onto the detector set-up or increasing the distance d between the two detector layers. The simulated distance $d = 5$ mm, causes a relative poor angular resolution resulting from the position resolution of the detectors. A larger distance reduces the number of total events but increases the angular resolution and therefore improves the event selection. The methods mentioned so far focus on increasing the signal rate. An additional improvement of the background exclusion also increases the SNR. A possibility could be an anti-coincidence shield around the detector set-up. Unfortunately, this would implicate a significant reduction of the calorimeter size and therefore a reduction of signal events with strong polarization dependence.

In summary, this thesis proves that ComPol's sensitivity on polarization is at the order of magnitude which is expected to observe Cygnus X-1 ($P \lesssim 25\%$). The following methods are proposed for future design studies: extension of the event selection to further event types, optimization of the geometry (e.g. distance between the detectors), and surrounding the detector system with an anti-coincidence shield to reduce the background.

Appendix A

Geometry description for the Geant4 simulation

The tables A.1 to A.6 list all information about the different detector parts, shown in figure 3.1. The tables contain the dimensions of the different volumes, their materials, their mass, and information regarding the position in the set-up if necessary. Table A.9 contains an estimation for the mass of the complete 3 unit CubeSat.

The whole geometry describes a simplified model of the final ComPol satellite. The actual 3 unit CubeSat is shrunk down to only one unit. It is mostly confined by the CubeSat structure (table A.5). Only a lead tube used as a collimator (table A.3) protrudes from the volume, defined by this aluminum structure. The side of the satellite with the protruding collimator is defined as the front side. The collimator and all following volumes except for the solar panels are centered with regard to the longitudinal axis of the CubeSat (parallel to the thicker rods of the aluminum structure). The front side except for a hole for the collimator is filled out by a lead shielding (table A.4). The collimator end in the CubeSat sits flush with the entrance window of the SDD. Behind the SDD (table A.1) is a 5 mm gap which is enclosed by the SDD and the calorimeter (table A.2). The material distribution of the real CubeSat is simplified by a dummy material block (tables A.7 and A.8) consisting of different material layers. The amount of each material is roughly estimated from the description of the CubeSat components in [29]. The thickness of each layer and its material are listed in table A.7. This material block is placed behind the detector system with a distance of 10 mm to the calorimeter. The layers are in the same order as in table A.7. All four side surfaces of the CubeSat are covered with solar panels (table A.6). In figure 3.1, most of these panels are transparent, to show the internal structure of the geometry.

For reproducibility, a section of the Geant4 code is added to the geometry description. This code contains the Geant4 material definitions used for the simulation.

Table A.1:
SDD configuration

Attribute	Implementation
Material	Silicon
Width	10 mm
Thickness	0.4 mm
Mass	0.1 g
Distance d*	5 mm

*distance to the calorimeter

Table A.2:
Calorimeter configuration

Attribute	Implementation
Material	CeBr ₃
Width	80 mm
Thickness	10 mm
Mass	333 g
Distance d*	5 mm

*distance to the SDD

Table A.3:
Collimator configuration

Attribute	Implementation
Material	Lead
Total length	100 mm
Protruding length	60 mm
Inner radius	7.5 mm
Outer radius	10 mm
Mass	156 g

Table A.4:

Front shielding configuration

Attribute	Implementation
Material	Lead
Width	83 mm
Thickness	2 mm
Mass	149 g

Table A.5:

CubeSat structure configuration

Attribute	Implementation
Material	Aluminum
Total width	100 mm
Total length	113.5 mm
Rod size*	8.5 mm, 5.7 mm
Indentation**	6.5 mm
Mass per unit	146 g

*for lengthwise, crosswise rods

**of crosswise rods from the front/back side

Table A.6:

Solar panel configuration

Attribute	Implementation
Cell material	GaAs
Substrate mat.	Polyimide
Cell thickness	0.8 mm
Substrate thickness	1.6 mm
Mass per panel	46 g

Table A.7:
 Dummy material distribution
 of the final CubeSat:
 Layer thickness

Material	Thickness (mm)	Mass (g)
Silicon	0.2	3.0
Aluminium	1.0	17.3
Lithium	10.0	34.2
PCB*	8.0	94.7
Copper	3.0	172.0
Iron	8.0	403.1
Aluminum	6.0	103.6

*material of printed circuit boards (PCB)

Table A.8:
 Dummy material distribution
 of the final CubeSat:
 Further configuration

Attribute	Implementation
Width	80 mm
Gap*	10 mm

*between dummy materials and calorimeter

Table A.9:
 Total mass of the 3 unit CubeSat

Component	Mass (g)
Detectors	333
Shielding	305
Dummy material dist.	828
Structure	438
Solar panels	553
Total	2457

Code section of the used Geant4 material definitions

```
#include <G4SystemOfUnits.hh>
#include <G4NistManager.hh>
#include <G4Material.hh>
#include <G4MaterialTable.hh>
#include <G4Element.hh>
#include <G4ElementTable.hh>

G4NistManager* nist = G4NistManager::Instance();

G4double density, z;
G4int natoms, nComponents;
G4String name, symbol;

// ----- Material definition -----

// Silicon
G4Material* Si = nist->FindOrBuildMaterial("G4_Si");

// CeBr3
G4Element* elCe = new G4Element(name="Cer", symbol="Ce", z=58.,
    140.12*g/mole);
G4Element* elBr = new G4Element(name="Brom", symbol="Br", z=35.,
    79.904*g/mole);
density = 5.2*g/cm3;
G4Material* CeBr3 = new G4Material("CeBr3", density, nComponents=2);
CeBr3->AddElement(elCe, natoms=1);
CeBr3->AddElement(elBr, natoms=3);

// Lead
G4Material* Pb = nist->FindOrBuildMaterial("G4_Pb");

// Aluminum
G4Material* Al = nist->FindOrBuildMaterial("G4_Al");

// Lithium
G4Material* Li = nist->FindOrBuildMaterial("G4_Li");
```

```

// PCB material (epoxy resin (C21H25ClO5) and glasfibre (SiO2))
G4Element* elC = new G4Element(name="Carbon", symbol="C", z=6., 12.01*
    g/mole);
G4Element* elH = new G4Element(name="Hydrogen", symbol="H", z=1.,
    1.00*g/mole);
G4Element* elCl = new G4Element(name="Chlorine", symbol="Cl", z=17.,
    35.45*g/mole);
G4Element* elO = new G4Element(name="Oxygen", symbol="O", z=8., 16.00*
    g/mole);
G4Element* elSi = new G4Element(name="Silicon", symbol="Si", z=14.,
    28.09*g/mole);
density = 1.85*g/cm3;
G4Material* PCB = new G4Material("PCB", density, nComponents=5);
PCB->AddElement(elC, natoms=63);
PCB->AddElement(elH, natoms=75);
PCB->AddElement(elCl, natoms=3);
PCB->AddElement(elO, natoms=119);
PCB->AddElement(elSi, natoms=52);

// Copper
G4Material* Cu = nist->FindOrBuildMaterial("G4_Cu");

// Iron
G4Material* Fe = nist->FindOrBuildMaterial("G4_Fe");

// GaAs (for solar cells)
G4Element* elGa = new G4Element(name="Gallium", symbol="Ga", z=31.,
    69.72*g/mole);
G4Element* elAs = new G4Element(name="Arsenic", symbol="As", z=33.,
    74.92*g/mole);
density = 5.32*g/cm3;
G4Material* GaAs = new G4Material("GaAs", density, nComponents=2);
GaAs->AddElement(elGa, natoms=1);
GaAs->AddElement(elAs, natoms=1);

// Polyimide (C35H28N2O7) (substrate of solar panels)
G4Element* elN = new G4Element(name="Nitrogen", symbol="N", z=7.,
    14.01*g/mole);
density = 1.42*g/cm3;
G4Material* Polyimide = new G4Material("Polyimide", density,
    nComponents=4);

```

```
Polyimide->AddElement(e1C, natoms=35);  
Polyimide->AddElement(e1H, natoms=28);  
Polyimide->AddElement(e1N, natoms=2);  
Polyimide->AddElement(e1O, natoms=7);
```

Appendix B

Normalization of the simulation results

The quantitative results X_{sim} from the simulation have to be normalized to obtain a meaningful statement on the expected value X_{real} in the real world. The normalization is done like it is shown in equation B.1.

$$X_{\text{real}} = X_{\text{sim}} \frac{N_{\text{real}}}{N_{\text{sim}}} \quad (\text{B.1})$$

The number of simulated events is expressed as N_{sim} and the number of expected events in the real world as N_{real} .

For the signal simulation it is an easy task to determine N_{real} :

$$N_{\text{real}} = F_{\text{Cyg}} \cdot A_{\text{SDD}} \cdot t . \quad (\text{B.2})$$

The total particle flux of Cygnus X-1 in the simulated energy range (10 keV to 300 keV) is labeled with F_{Cyg} . It is equal to the spectrum in figure 3.2 integrated over the energy. The simulated source exactly illuminates the complete SDD. Therefore, A_{SDD} is the area of the silicon detector. The time t determines the time to which the simulation result is normalized to.

The calculation for the background simulation with isotropic radiation is more complex. The particles originate from a spherical surface with radius R_s . An important setting to obtain isotropic radiation inside the sphere is the cosine emission law of Geant4. The need of this setting is visualized in figure B.1. To do the correct normalization it is necessary to calculate the number of events, that penetrate a sphere with radius R_s in reality. The background spectra are given as differential flux $\frac{dF_{\text{Bg}}}{dE}$ per solid angle ($\text{cm}^{-2} \text{s}^{-1} \text{sr}^{-1} \text{keV}^{-1}$). The effective solid angle Ω_{eff} covered by one point on the sphere surface under cosine emission is calculated with equation B.3.

$$\Omega_{\text{eff}} = \int_0^{2\pi} d\phi \int_0^{\frac{\pi}{2}} d\theta \cos \theta \sin \theta = \pi \quad (\text{B.3})$$

The final number N_{real} of expected events in real conditions results as:

$$N_{\text{real}} = F_{\text{bg}} \cdot \Omega_{\text{eff}} \cdot A_s \cdot t = F_{\text{bg}} 4\pi^2 R_s^2 t \quad (\text{B.4})$$

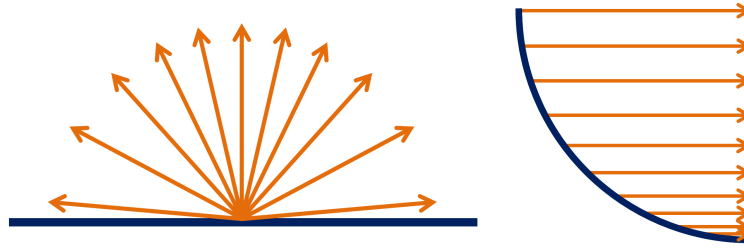


Figure B.1: Visualization of the cosine emission law.

Left: Emission from a plane surface according to the cosine emission law.

Right: The radiation inside a sphere is not isotropic, when the emission from the sphere surface is not according to the cosine emission law.

with the sphere surface $A_s = 4\pi R_s^2$ and F_{bg} as the differential background rate integrated over the energy.

Appendix C

Energy spectra of both detectors

C.1 Monoenergetic photon sources

The figures C.1, C.3, C.5 and C.7 show the spectra of the silicon detector for simulations with different monoenergetic photon beams (Used energies: 30 keV, 100 keV, 150 keV, and 300 keV). The spectra of the calorimeter for the same energies are shown in figures C.2, C.4, C.6 and C.8.

General description for all plotted spectra:

The total spectrum is always plotted as a gray area. Each event is assigned to a spectral component according to the respective classification for the SDD or for the calorimeter (introduced in section 3.4.1 and 3.4.2). Visualizations of the event types for the silicon detector are shown in figure 3.5 and 3.6. The event types of the calorimeter are covered by figure 3.9 and 3.10. The distribution for each event type is plotted separately again. Resolutions and thresholds of the detectors are not taken into account.

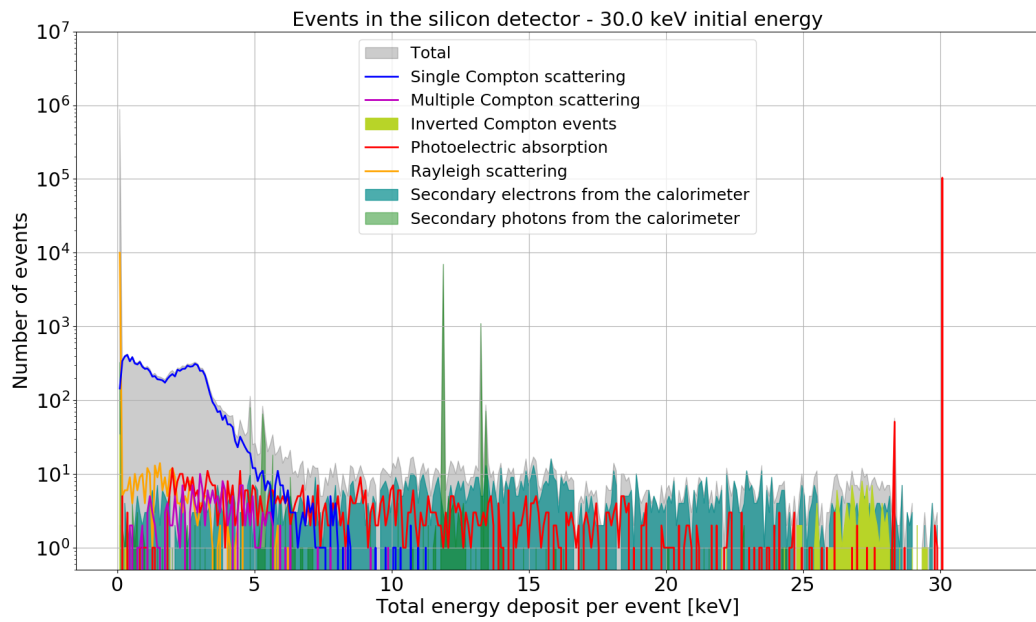


Figure C.1: Simulated spectrum of the SDD for a 30 keV photon beam.

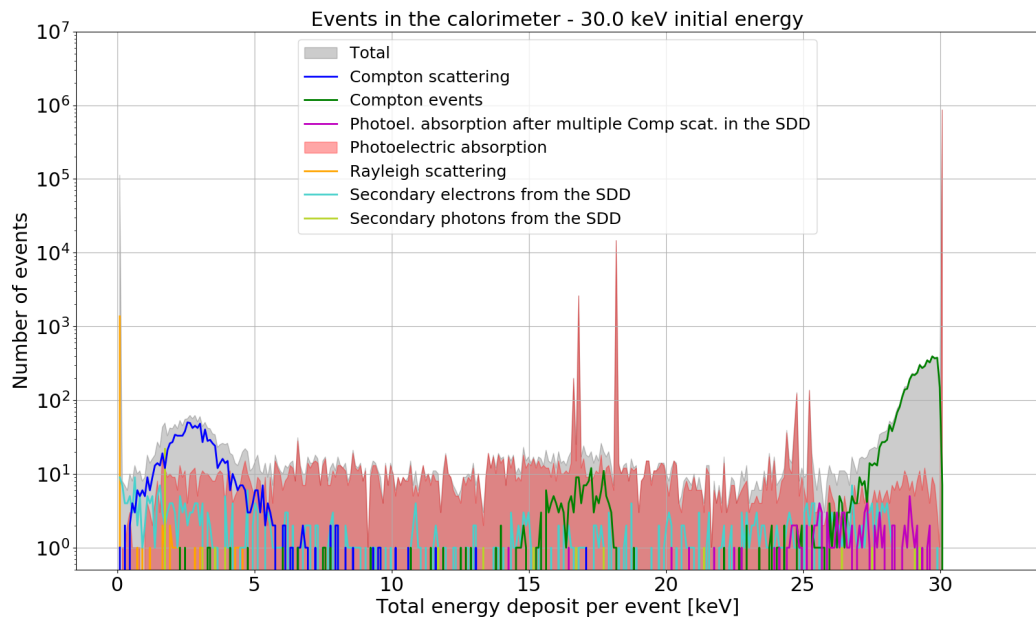


Figure C.2: Simulated spectrum of the calorimeter for a 30 keV photon beam.

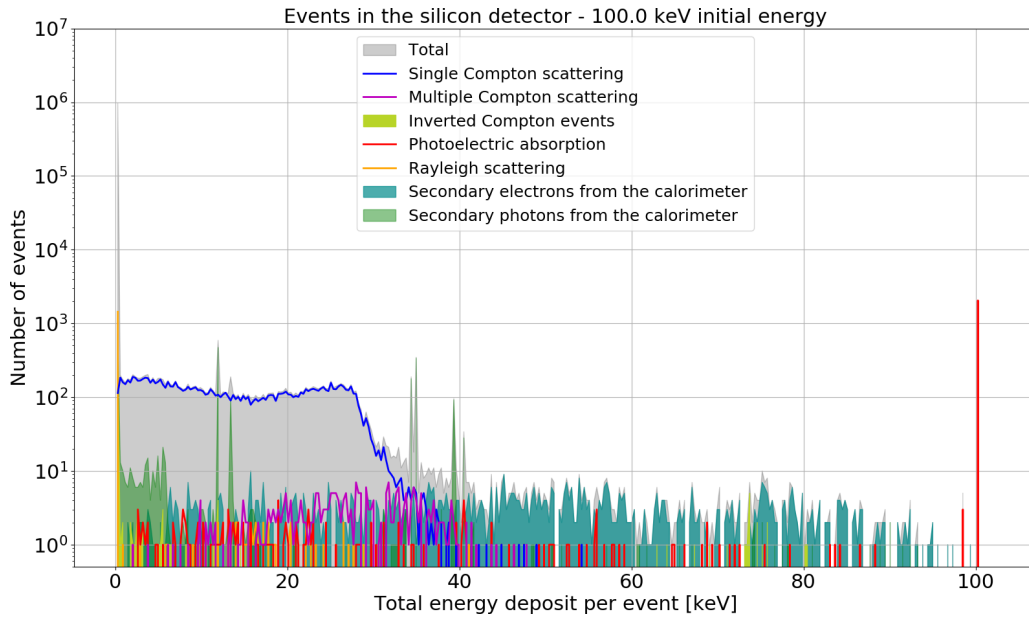


Figure C.3: Simulated spectrum of the SDD for a 100 keV photon beam.

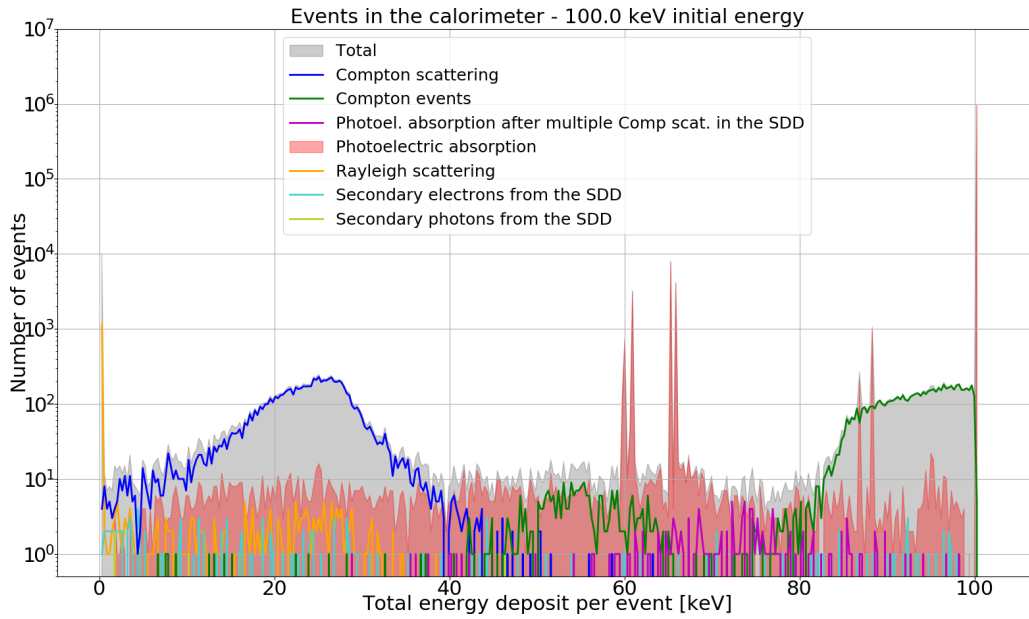


Figure C.4: Simulated spectrum of the calorimeter for a 100 keV photon beam.

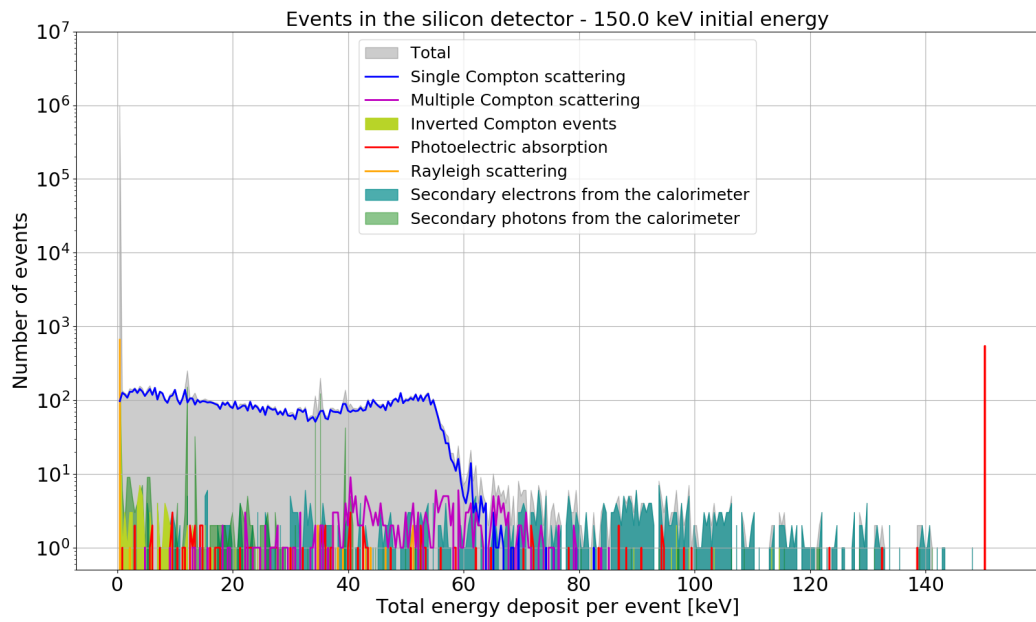


Figure C.5: Simulated spectrum of the SDD for a 150 keV photon beam.

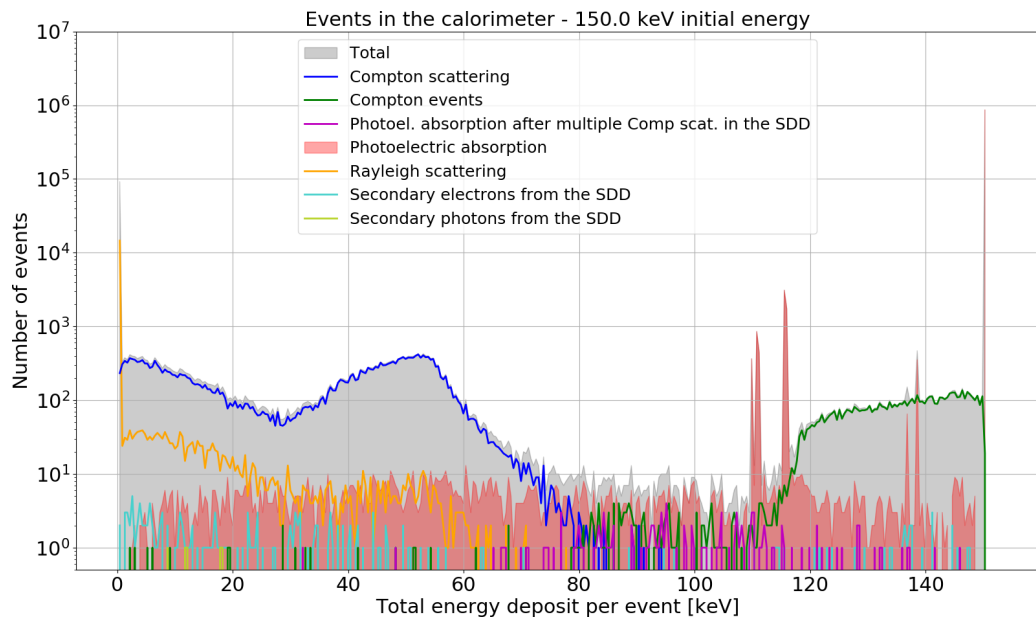


Figure C.6: Simulated spectrum of the calorimeter for a 150 keV photon beam.

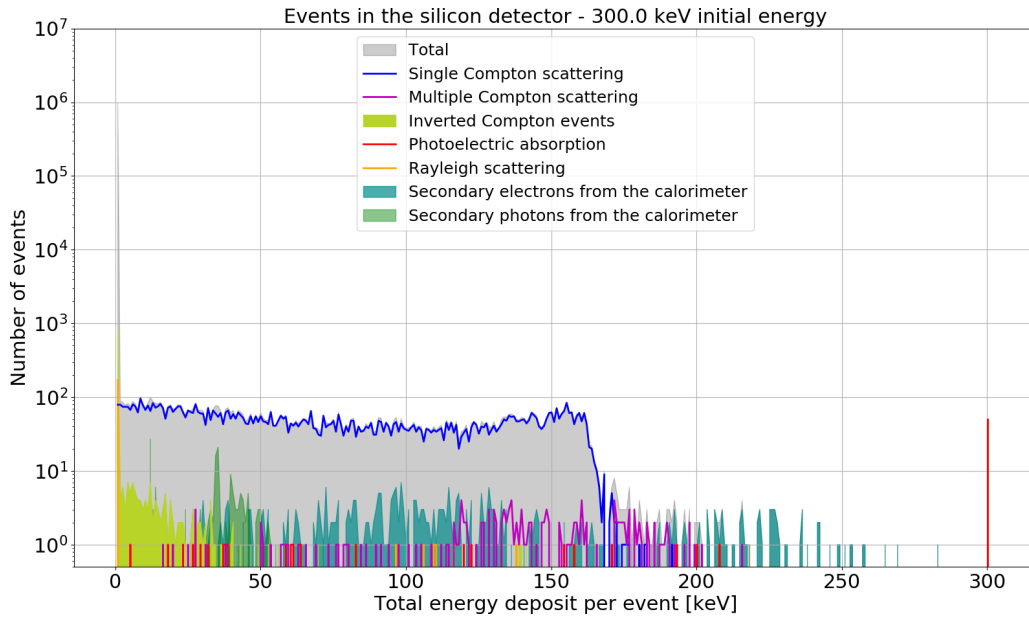


Figure C.7: Simulated spectrum of the SDD for a 300 keV photon beam.

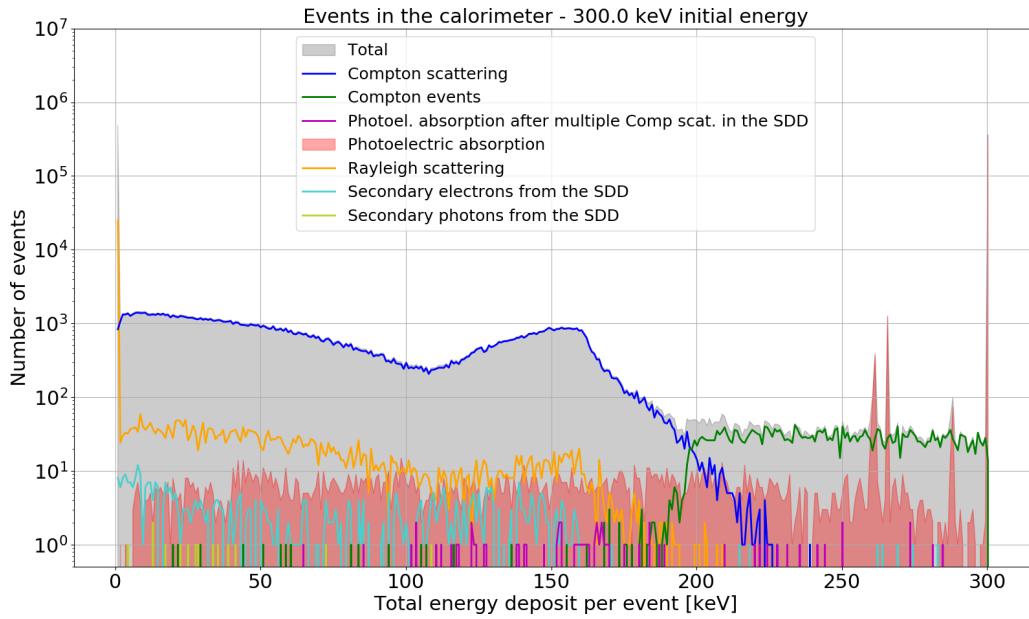


Figure C.8: Simulated spectrum of the calorimeter for a 300 keV photon beam.

C.2 Photon source with spectrum of Cygnus X-1

Figure C.9 shows the spectrum of the silicon detector for a simulation with an initial energy distribution according to the spectrum of Cygnus X-1. The equivalent spectrum of the calorimeter is shown in figure C.10.

General description for the two plotted spectra:

The total spectrum is plotted as a gray area. Each event is assigned to a spectral component according to the respective classification for the SDD or for the calorimeter (introduced in section 3.4.1 and 3.4.2). Visualizations of the event types for the silicon detector are shown in figure 3.5 and 3.6. The event types of the calorimeter are covered by figure 3.9 and 3.10. The distribution for each event type is plotted separately again. Resolutions and thresholds of the detectors are not taken into account.

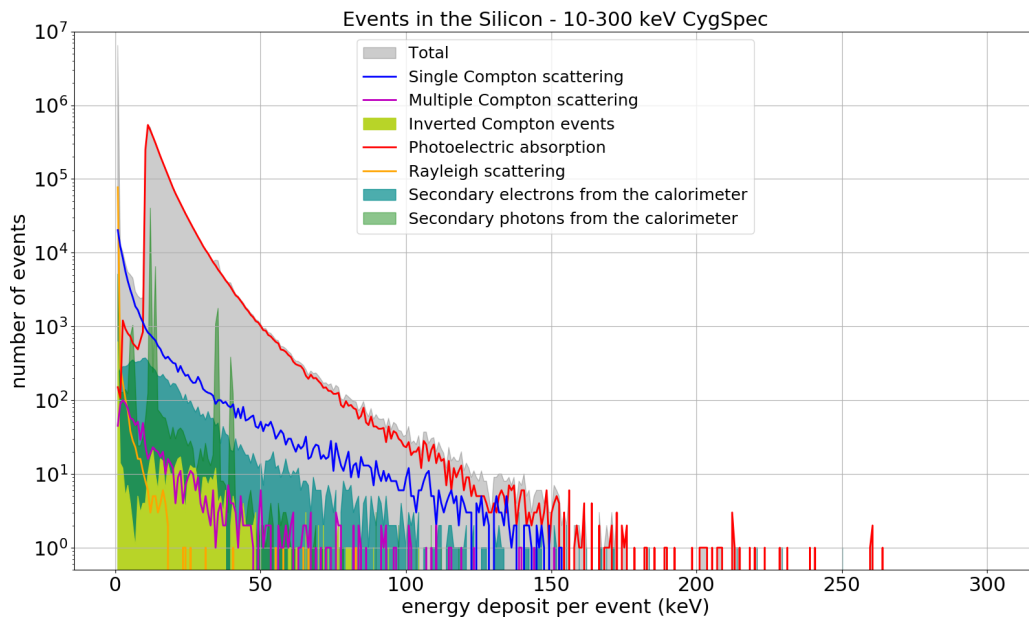


Figure C.9: Simulated spectrum of the SDD for an initial energy distribution according to the spectrum of Cygnus X-1.

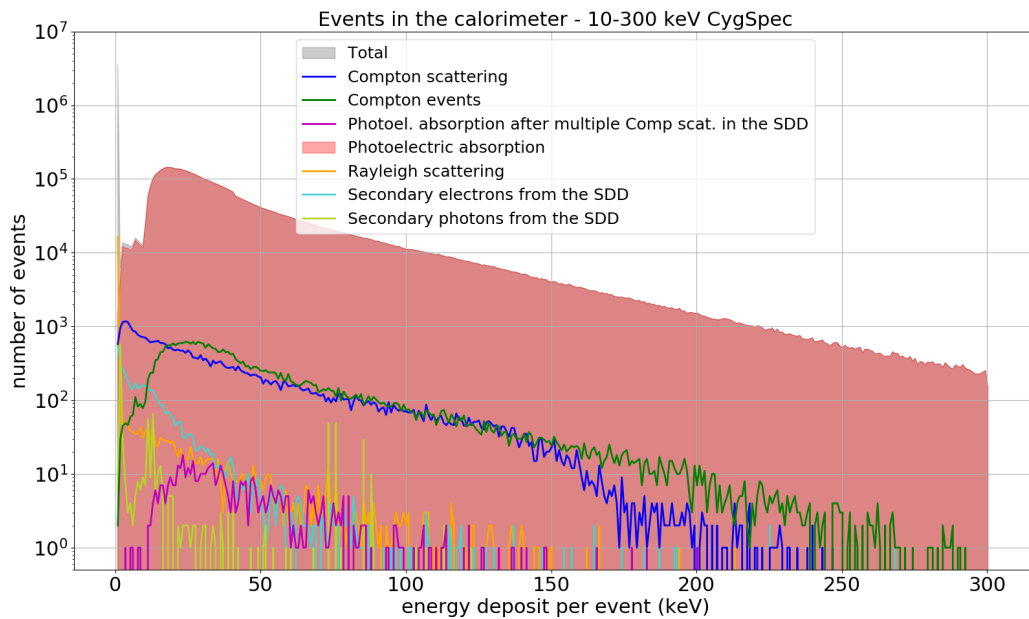


Figure C.10: Simulated spectrum of the calorimeter for an initial energy distribution according to the spectrum of Cygnus X-1.

C.3 Background spectra

Figure C.11 and C.12 show the spectra of the silicon detector and the calorimeter for the background simulation. Both times, the total spectrum is plotted in gray. The colored lines display the contributions for the different initial particle types.

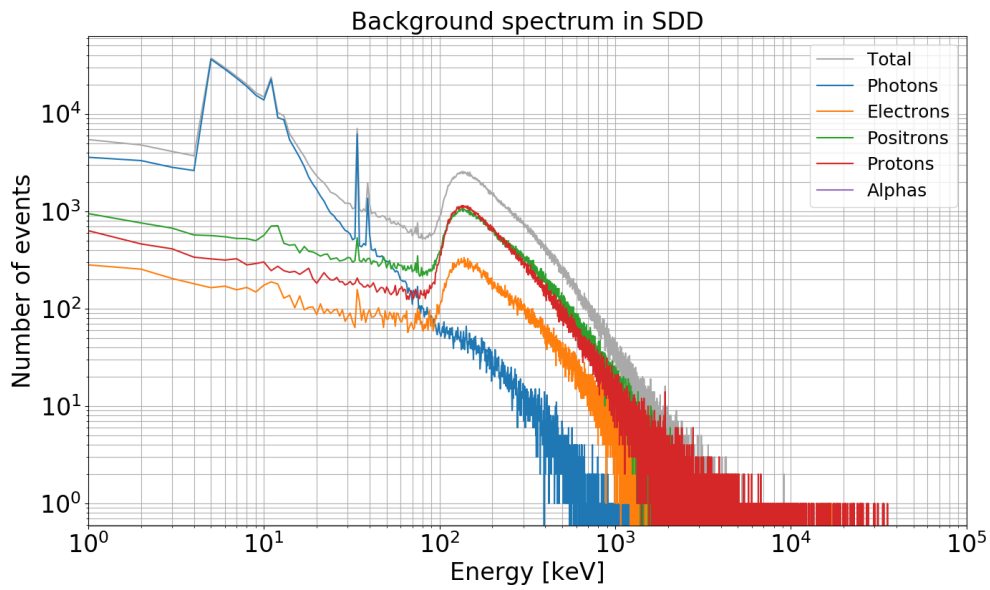


Figure C.11: Simulated spectrum of the SDD from the background simulation.

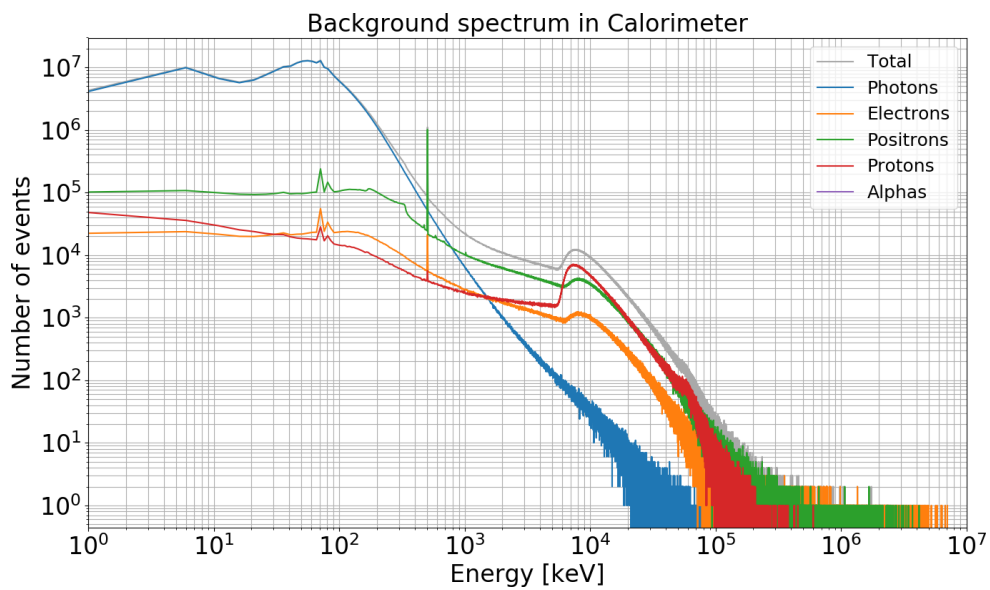


Figure C.12: Simulated spectrum of the calorimeter from the background simulation.

Bibliography

- [1] The New York Times. <https://www.nytimes.com/2018/03/14/world/europe/stephen-hawking-quotes.html>, Nov. 2019.
- [2] M. Berger, J. Hubbell, et al. XCOM: Photon cross sections database (version 1.5), 2010. URL <https://dx.doi.org/10.18434/T48G6X>.
- [3] C. Powell. X-ray Photoelectron Spectroscopy Database XPS, Version 4.1, NIST Standard Reference Database 20, 1989. URL <https://dx.doi.org/10.18434/T4T88K>.
- [4] W. R. Leo. *Techniques for nuclear and particle physics experiments: A how-to approach ; with 40 tables and numerous worked examples*. Springer, Berlin, 2., rev. ed. edition, 1994. ISBN 978-3-540-57280-0.
- [5] O. Klein and Y. Nishina. Über die Streuung von Strahlung durch freie Elektronen nach der neuen relativistischen Quantendynamik von Dirac. *Zeitschrift für Physik*, 52(11-12):853–868, 1929. ISSN 0044-3328. doi:10.1007/BF01366453.
- [6] J. H. Hubbell, Wm. J. Veigle, et al. Atomic form factors, incoherent scattering functions, and photon scattering cross sections. *Journal of Physical and Chemical Reference Data*, 4(3):471–538, 1975. ISSN 0047-2689. doi:10.1063/1.555523.
- [7] T. E. Strohmayer and T. R. Kallman. ON THE STATISTICAL ANALYSIS OF X-RAY POLARIZATION MEASUREMENTS. *The Astrophysical Journal*, 773(2):103, 2013. ISSN 0004-637X. doi:10.1088/0004-637X/773/2/103.
- [8] Max-Planck-Institut für extraterrestrische Physik. https://www.mpe.mpg.de/27826/Compton_GRO, Nov. 2019.
- [9] V. Schonfelder, R. Diehl, et al. The Imaging Compton Telescope Comptel on the Gamma Ray Observatory. *IEEE Transactions on Nuclear Science*, 31(1):766–770, 1984. ISSN 0018-9499. doi:10.1109/TNS.1984.4333363.
- [10] European Space Agency (ESA). <https://www.cosmos.esa.int/web/integral/instruments-ibis>, Nov. 2019. Cosmos portal.

- [11] M. J. Reid, J. E. McClintock, et al. THE TRIGONOMETRIC PARALLAX OF CYGNUS X-1. *The Astrophysical Journal*, 742(2):83, 2011. ISSN 0004-637X. doi:10.1088/0004-637X/742/2/83.
- [12] J. Ziółkowski. Determination of the masses of the components of the HDE 226868/Cyg X-1 binary system. *Monthly Notices of the Royal Astronomical Society: Letters*, 440(1):L61–L65, 2014. ISSN 1745-3925. doi:10.1093/mnrasl/slu002.
- [13] J. LaSala, P. A. Charles, et al. The orbital period of HDE 226868/Cyg X-1. *Monthly Notices of the Royal Astronomical Society*, 301(1):285–288, 1998. ISSN 0035-8711. doi:10.1046/j.1365-8711.1998.02064.x.
- [14] V. Grinberg, N. Hell, et al. Long term variability of Cygnus X-1. *Astronomy & Astrophysics*, 554:A88, 2013. ISSN 0004-6361. doi:10.1051/0004-6361/201321128.
- [15] F. Cangemi and J. others Rodriguez. High energy spectral study of the black hole Cygnus X-1 with INTEGRAL, 2018. URL <http://arxiv.org/abs/arXiv:1810.12049>.
- [16] J. M. Paredes, F. A. Aharonian, et al. Gamma rays from compact binary systems. In *AIP Conference Proceedings*, pages 157–168. AIP, 2008. doi:10.1063/1.3076631.
- [17] J. Wilms, M. A. Nowak, et al. Long term variability of Cygnus X-1. *Astronomy & Astrophysics*, 447(1):245–261, 2006. ISSN 0004-6361. doi:10.1051/0004-6361:20053938.
- [18] P. Laurent and L. Titarchuk. The Converging Inflow Spectrum Is an Intrinsic Signature for a Black Hole: Monte Carlo Simulations of Comptonization on Free-falling Electrons. *The Astrophysical Journal*, 511(1):289, 1999. ISSN 0004-637X. doi:10.1086/306683.
- [19] P. Laurent, J. Rodriguez, J. Wilms, et al. Polarized gamma-ray emission from the galactic black hole Cygnus X-1. *Science (New York, N.Y.)*, 332(6028):438–439, 2011. doi:10.1126/science.1200848.
- [20] M. L. McConnell, A. A. Zdziarski, et al. The Soft Gamma-Ray Spectral Variability of Cygnus X-1. *The Astrophysical Journal*, 572(2):984–995, 2002. ISSN 0004-637X. doi:10.1086/340436.
- [21] G. E. Romero, F. L. Vieyro, and S. Chaty. Coronal origin of the polarization of the high-energy emission of Cygnus X-1. *Astronomy & Astrophysics*, 562:L7, 2014. ISSN 0004-6361. doi:10.1051/0004-6361/201323316.

- [22] P. Meszaros, R. Novick, et al. Astrophysical implications and observational prospects of X-ray polarimetry. *The Astrophysical Journal*, 324:1056, 1988. ISSN 0004-637X. doi:10.1086/165962.
- [23] H. Krawczynski, A. Garson, et al. Scientific prospects for hard X-ray polarimetry. *Astroparticle Physics*, 34(7):550–567, 2011. ISSN 09276505. doi:10.1016/j.astropartphys.2010.12.001.
- [24] E. Agol and J. H. Krolik. Magnetic Stress at the Marginally Stable Orbit: Altered Disk Structure, Radiation, and Black Hole Spin Evolution. *The Astrophysical Journal*, 528(1):161–170, 2000. ISSN 0004-637X. doi:10.1086/308177.
- [25] J. D. Schnittman and J. H. Krolik. X-RAY POLARIZATION FROM ACCRETING BLACK HOLES: THE THERMAL STATE. *The Astrophysical Journal*, 701(2):1175–1187, 2009. ISSN 0004-637X. doi:10.1088/0004-637X/701/2/1175.
- [26] J. Rodriguez, V. Grinberg, et al. SPECTRAL STATE DEPENDENCE OF THE 0.4–2 MEV POLARIZED EMISSION IN CYGNUS X-1 SEEN WITH INTEGRAL/IBIS, AND LINKS WITH THE AMI RADIO DATA. *The Astrophysical Journal*, 807(1):17, 2015. ISSN 0004-637X. doi:10.1088/0004-637X/807/1/17.
- [27] European Space Agency (ESA). <https://sci.esa.int/web/integral/-/48589-cygnus-x-1-s-energy-spectrum-and-polarized-signal>, Nov. 2019.
- [28] J. Chin, R. Coelho, et al. https://www.nasa.gov/sites/default/files/atoms/files/nasa_csli_cubesat_101_508.pdf, 2017. NASA CubeSat Launch Initiative.
- [29] M. Agnan, J. Vannitsen, and Y.-P. Tsai. Feasibility Study for the COMPOL Mission. Technical report, ODYSSEUS Space Inc., 2018.
- [30] S. Mertens, T. Lasserre, et al. Sensitivity of next-generation tritium beta-decay experiments for keV-scale sterile neutrinos. *Journal of Cosmology and Astroparticle Physics*, 2015(02):020, 2015. ISSN 1475-7516. doi:10.1088/1475-7516/2015/02/020.
- [31] M. Aker, K. Altenmüller, et al. Improved Upper Limit on the Neutrino Mass from a Direct Kinematic Method by KATRIN. *Physical Review Letters*, 123(22), 2019. ISSN 0031-9007. doi:10.1103/PhysRevLett.123.221802.
- [32] J. Angrik, T. Armbrust, et al. KATRIN design report 2004. Technical report, Forschungszentrum, Karlsruhe, 2005. 51.54.01; LK 01.
- [33] S. Mertens, A. Alborini, et al. A novel detector system for KATRIN to search for keV-scale sterile neutrinos. *Journal of Physics G: Nuclear and Particle Physics*, 46(6):065203, 2019. ISSN 1367-2630. doi:10.1088/1361-6471/ab12fe.

- [34] D. Siegmann. Investigation of the Detector Response to Electrons of the TRISTAN Prototype Detectors. Master’s thesis, Technical University of Munich, Munich, 2019.
- [35] W. M. Higgins, A. Churilov, et al. Crystal growth of large diameter LaBr₃:Ce and CeBr₃. *Journal of Crystal Growth*, 310(7-9):2085–2089, 2008. ISSN 00220248. doi:10.1016/j.jcrysgro.2007.12.041.
- [36] A. Gostojić. *Development of a Compton Telescope with 3D Imaging Calorimeter for Gamma-Ray Astronomy*. PhD thesis, Université Paris-Saclay, Paris-Saclay, 2016.
- [37] W. Ley, K. Wittmann, and W. Hallmann. *Handbuch der Raumfahrttechnik*. Carl Hanser Verlag GmbH & Co. KG, München, 2019. ISBN 978-3-446-45429-3. doi:10.3139/9783446457232.
- [38] F. Perotti and C. Fiorini. Observed energy dependence of Fano factor in silicon at hard X-ray energies. *Nuclear Instruments and Methods in Physics Research Section A: Accelerators, Spectrometers, Detectors and Associated Equipment*, 423(2-3):356–363, 1999. ISSN 01689002. doi:10.1016/S0168-9002(98)01264-9.
- [39] T. Brunst, S. Mertens, et al. Development of a silicon drift detector system for the TRISTAN project—Future search for sterile neutrinos. *Nuclear Instruments and Methods in Physics Research Section A: Accelerators, Spectrometers, Detectors and Associated Equipment*, 936:235–236, 2019. ISSN 01689002. doi:10.1016/j.nima.2018.09.116.
- [40] Geant4 Collaboration. <https://geant4.web.cern.ch/>, Nov. 2019.
- [41] P. Cumani, M. Hernanz, et al. Background for a gamma-ray satellite on a low-Earth orbit. *Experimental Astronomy*, 47(3):273–302, 2019. ISSN 1572-9508. doi:10.1007/s10686-019-09624-0.
- [42] F. Muleri and R. Campana. SENSITIVITY OF STACKED IMAGING DETECTORS TO HARD X-RAY POLARIZATION. *The Astrophysical Journal*, 751(2):88, 2012. ISSN 0004-637X. doi:10.1088/0004-637X/751/2/88.
- [43] C. W. Stearns, D. L. McDaniel, et al. Random coincidence estimation from single event rates on the Discovery ST PET/CT scanner. In *2003 IEEE Nuclear Science Symposium Conference*, pages 3067–3069, [Place of publication not identified], 2004. I E E E. ISBN 0-7803-8257-9. doi:10.1109/NSSMIC.2003.1352545.
- [44] M. C. Weisskopf. *X-ray polarimetry: historical remarks and other considerations*, page 1–8. Cambridge Contemporary Astrophysics. Cambridge University Press, 2010. doi:10.1017/CBO9780511750809.002.

Declaration of Authorship

English:

I hereby declare that I have written the present Master thesis in the course Nuclear, Particle and Astrophysics independently only using the cited external resources.

German:

Ich erkläre hiermit, dass ich die vorliegende Abschlussarbeit im Masterstudiengang Kern-, Teilchen und Astrophysik selbstständig und nur mit den angegebenen Hilfsmitteln angefertigt habe.

Matthias Meier,
Munich, December 2nd, 2019

Acknowledgments

I would like to thank everyone who supported me during my master thesis, in particular:

- Prof. Dr. Susanne Mertens for the opportunity to learn a lot during the time in her group, for interesting discussions, and for the great trust and the responsibility I received for representing our project
- Thierry Lasserre for the trip to the CEA in Paris and for constructive discussions
- Daniel Maier and Philippe Laurent from the CEA for fruitful discussions, constructive feedback, and detailed answers to all my questions
- Thibaut Houdy for great discussions and support for all Geant4 related issues
- Korbinian Urban, Manuel Lebert and Christoph Köhler for the great atmosphere in our shared office and various interesting discussions
- All other members of the KATRIN/TRISTAN working group, especially those who helped me with proofreading my thesis
- And of course my family for their encouragement and help during this time